CHAPTER IV
RESULTS AND DISCUSSION

4.1 Photocatalyst Characterizations

4.1.1 TG-DTA Results

In order to determine the suitable calcination temperature and the thermal decomposition behavior of the synthesized $SrTi_xZr_{1-x}O_3$ photocatalysts, the TG-DTA analysis is a powerful technique normally used. The TG-DTA thermograms of the dried $SrTiO_3$, $SrTi_{0.9}Zr_{0.1}O_3$, and $SrZrO_3$ gels exhibit quite a similar thermal behavior, as shown in Figure 4.1. Two exothermic peaks and one endothermic peak are shown in the DTA curves which can be divided into three regions. The details of the peak regions and their corresponding weight losses are summarized in Table 4.1. The first region is ascribed to the removal of physisorbed water molecules, whereas the burnout process of the LAHC surfactant and the residual solvent take place in the second region. The third region is possibly attributed to the removal of remnant carbons and chemisorbed water, as well as the crystallization process of the photocatalysts and the decomposition of the remaining solvents that are tightly bound in the molecular level with Sr, Ti, and Zr metals in the gel network (Puangpetch et al., 2008). However, the temperature ranges of these regions of the $SrTi_xZr_{1-x}O_3$ photocatalysts with various Ti-to-Zr molar ratios are somewhat different because the interactions of Sr, Ti, and Zr species with the others in gel network may be different. From the TG curves, the weight loss of all the synthesized $SrTi_xZr_{1-x}O_3$ photocatalysts terminated at approximately 600°C, indicating that this temperature used for the calcination is sufficient for both the complete surfactant removal and the photocatalyst crystallization. Therefore, the calcination temperature in the range of 600 to 800°C was used to investigate its effect on the physicochemical properties and the consequent photocatalytic dye degradation activity.

Table 4.1 Thermal decomposition behavior of the dried synthesized SrTiO$_3$, SrTi$_{0.9}$Zr$_{0.1}$O$_3$, and SrZrO$_3$ photocatalysts from TG-DTA analysis

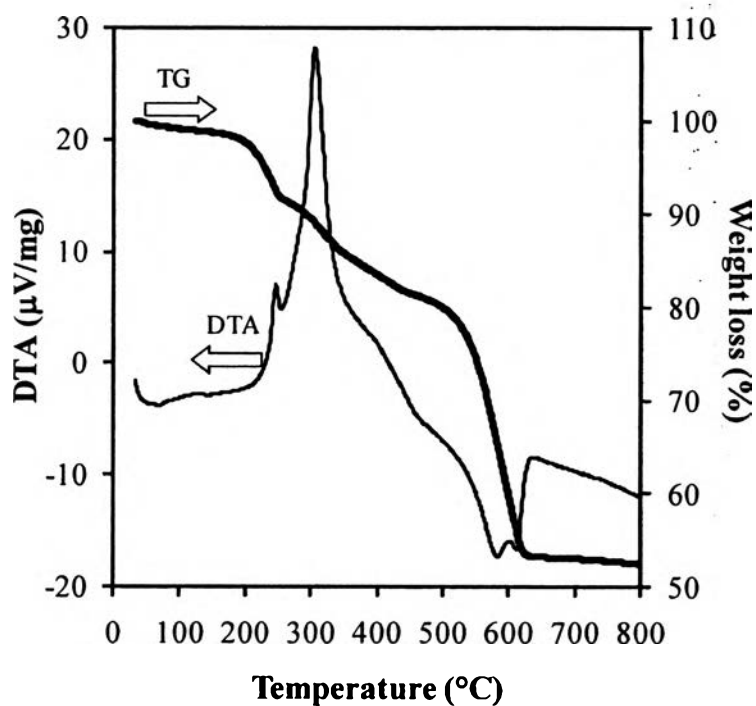| Photocatalyst	Exothermic peak				Endothermic peak		Total weight loss (%)
	Position (°C)		Weight loss (%)		Position (°C)	Weight loss (%)	
	1st region	2nd region	1st region	2nd region	3rd region	3rd region	
SrTiO$_3$	25-200	200-520	1.66	19.20	520-630	26.50	47.36
SrTi$_{0.9}$Zr$_{0.1}$O$_3$	25-190	190-525	3.40	23.00	525-630	21.05	47.45
SrZrO$_3$	25-180	180-550	4.85	25.40	550-630	16.12	46.37

(a)

Figure 4.1 TG-DTA curves of the dried synthesized (a) SrTiO$_3$, (b) SrTi$_{0.9}$Zr$_{0.1}$O$_3$, and (c) SrZrO$_3$ photocatalysts.

(b)
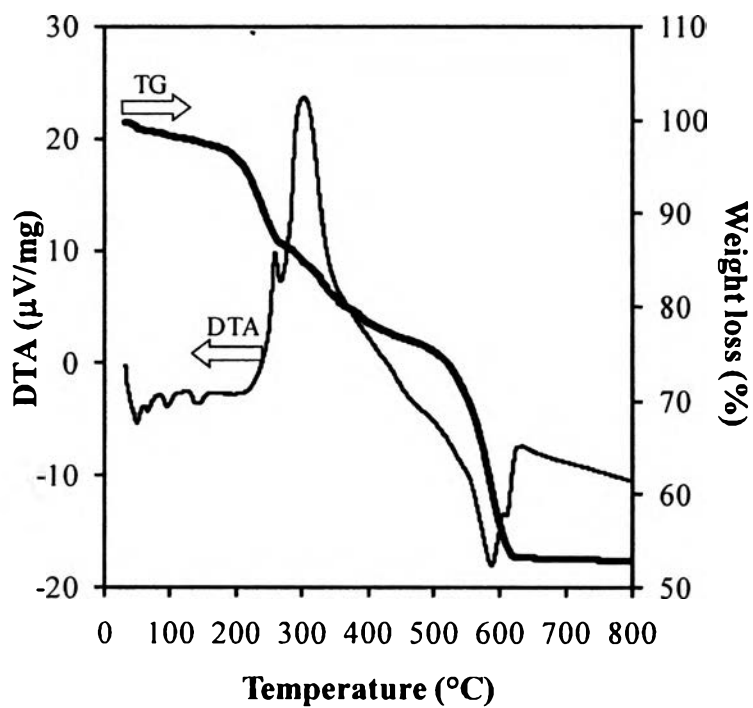
(c)

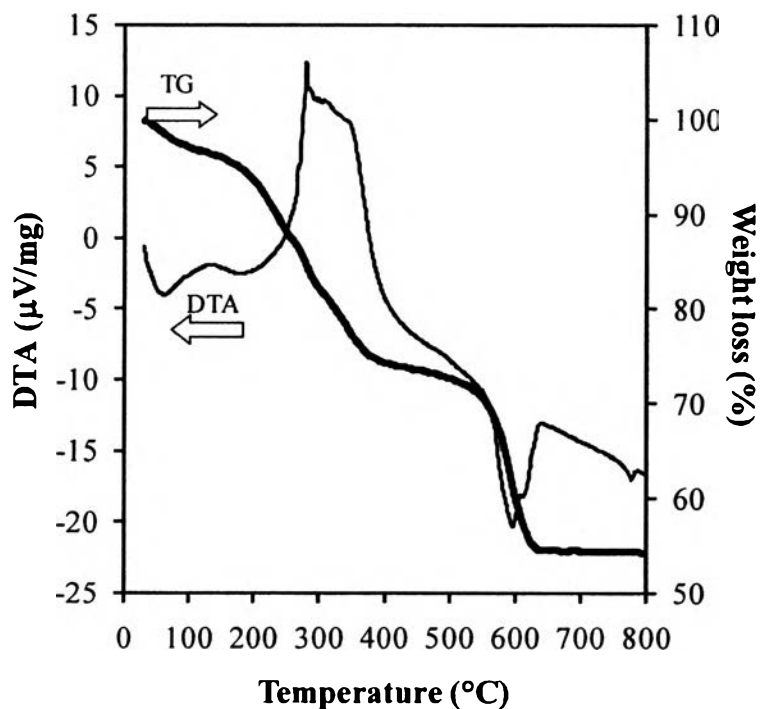**Figure 4.1 (Continued)** TG-DTA curves of the dried synthesized (a) $SrTiO_3$, (b) $SrTi_{0.9}Zr_{0.1}O_3$, and (c) $SrZrO_3$ photocatalysts.
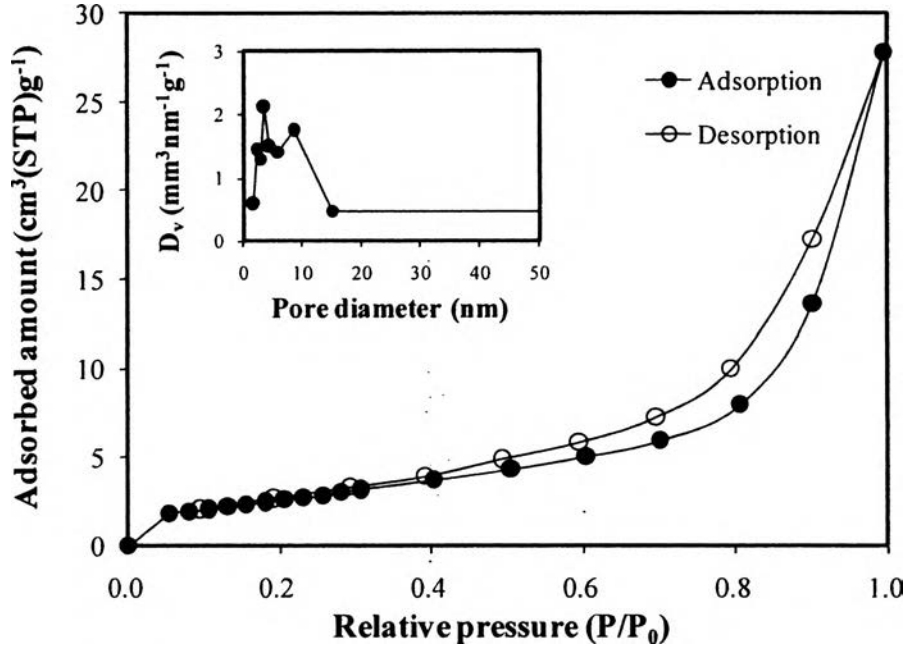
4.1.2 N$_2$ Adsorption-Desorption Results

The N$_2$ adsorption-desorption analysis is an important approach normally used to verify the mesoporosity of any studied materials. The characteristic behavior of the structure of powder, which is composed of an assembly of particles with large open packing, can be observed from the shape of the isotherms. Figure 4.2 depicts the exemplified N$_2$ adsorption-desorption isotherms and pore size distributions (insets) of the synthesized SrTiO$_3$, SrTi$_{0.9}$Zr$_{0.1}$O$_3$, and SrZrO$_3$ photocatalysts calcined at 700°C, and the synthesized 1.0 wt.% Pt-loaded mesoporous-assembled SrTi$_{0.9}$Zr$_{0.1}$O$_3$ photocatalyst calcined at 850°C. The isotherms of all the synthesized photocatalysts, except SrZrO$_3$, exhibited an IUPAC type IV-like pattern, indicating the existence of mesopores (mesoporous size between 2 and 50 nm) in their assembled frameworks, according to the classification of IUPAC (Rouquerol *et al.*, 1999). A sharp increase in adsorption volume of N$_2$ could be observed at high relative pressure (P/P$_0$). This sharp increase can be imputable to the capillary condensation of N$_2$ inside the mesopores, indicating the good homogeneity of the sample and fairly small pore size since the P/P$_0$ position of the inflection point is directly related to the pore dimension (Sreethawong *et al.*, 2005). However, the isotherms of the synthesized SrZrO$_3$ photocatalyst showed an IUPAC type III-like pattern due to the absence of a clear step increase in the amount of absorbed N$_2$ in the P/P$_0$ range of 0-0.05, indicating that its principal pore structure is not a mesopore. For the synthesized 1.0 wt.% Pt-loaded mesoporous-assembled SrTi$_{0.9}$Zr$_{0.1}$O$_3$ photocatalyst calcined at 850°C, which provided the highest photocatalytic performance for AB degradation as discussed later, its isotherms also exhibited an IUPAC type IV-like pattern. This implies that the Pt loading by the SSSG method did not significantly affect the mesoporous structure of the photocatalyst. Therefore, its mesoporous structure could be maintained. The pore size distributions of the synthesized photocatalysts as exemplified in the insets of Figure 4.2 reveal that all of the synthesized photocatalysts, except SrZrO$_3$, possessed narrow pore size distributions in the mesoporous region, confirming a good quality of the samples. Whereas, the pore size distribution of the synthesized SrZrO$_3$ photocatalyst tended to exist mainly in the microporous region (microporous size less than 2 nm). This may

be a possible explanation for the absence of a step increase in the absorbed N_2 amount at the low P/P_0 range due to the pore size obstruction.

The experimental results of the textural properties obtained from N_2 adsorption-desorption isotherms, including BET surface area, mean mesopore diameter, and total pore volume, of all the synthesized without and with Pt-loaded photocatalysts are summarized in Tables 4.2 and 4.3, respectively. For the synthesized mesoporous-assembled $SrTi_xZr_{1-x}O_3$ photocatalysts, the surface area, mean mesopore diameter, and total pore volume tended to initially increase with increasing Zr content to 10% ($SrTi_{0.9}Zr_{0.1}O_3$) and then gradually decreased with further increasing Zr content (Table 4.2). Then, the synthesized $SrTi_{0.9}Zr_{0.1}O_3$ photocatalyst was selected to further investigate the effects of calcination temperature, as compared to the synthesized $SrTiO_3$ photocatalyst, and calcination time. As clearly seen, the surface area, mean mesopore diameter, and total pore volume of the synthesized $SrTi_{0.9}Zr_{0.1}O_3$ photocatalysts tended to slightly increase with increasing calcination temperature until 700°C and then decreased with further increasing calcination temperature, whereas those of the synthesized $SrTiO_3$ photocatalysts tended to adversely decrease, except that the total pore volume remained almost unchanged. However, it was found that the calcination time did not significantly affect all of the textural properties. These results indicated a more dominant effect of the calcination temperature on the textural properties of the resulting products in this present work. It can be observed that the synthesized photocatalysts had a narrow range of mean mesopore diameter located between 3 to 16 nm, identifying a controlled pore size of the samples. For the synthesized Pt-loaded mesoporous-assembled $SrTi_{0.9}Zr_{0.1}O_3$ photocatalysts with various Pt loadings (Table 4.3), at any given calcination temperature, the increase in Pt loading did not significantly change the surface area and total pore volume, possibly due to its low loadings in the investigated range of 0-1.5 wt.%. However, the mean mesopore diameter shifted to lower value in the loading range of 1.2-1.5 wt.% at calcination temperatures lower than 800°C, whereas the mean mesopore diameter remained almost unchanged at all loadings at 800°C.
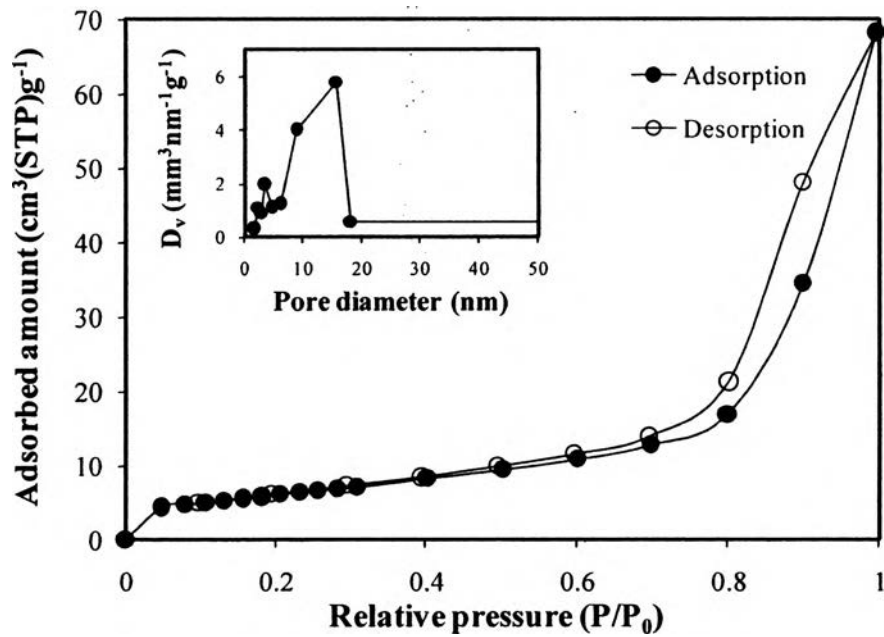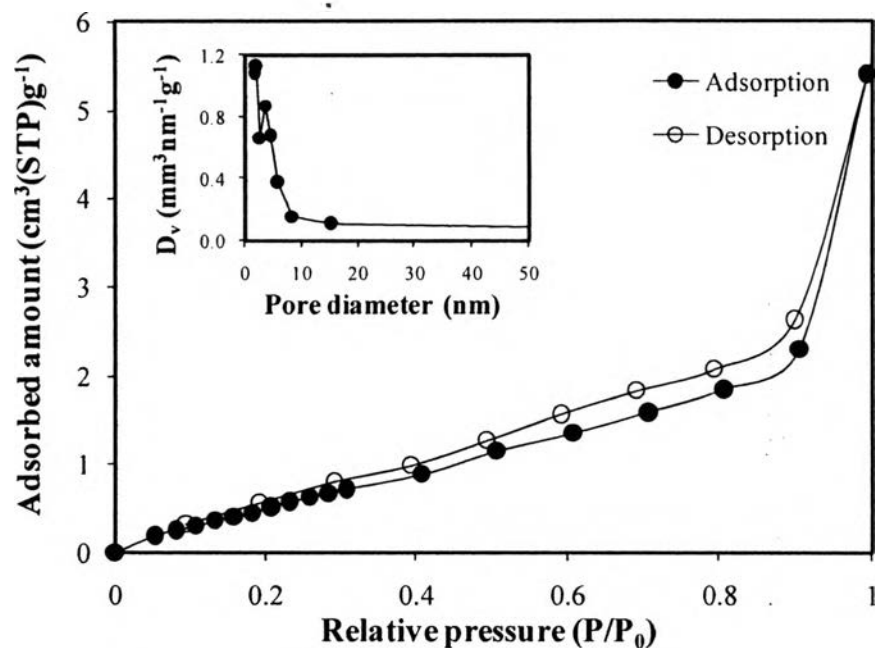
(a)

(b)

Figure 4.2 N_2 adsorption-desorption isotherms and pore size distributions (insets) of the synthesized (a) $SrTiO_3$, (b) $SrTi_{0.9}Zr_{0.1}O_3$, (c) $SrZrO_3$ photocatalysts calcined at 700°C for 4 h, and (d) the synthesized 1.0 wt.% Pt-loaded $SrTi_{0.9}Zr_{0.1}O_3$ photocatalyst calcined at 850°C for 4 h.
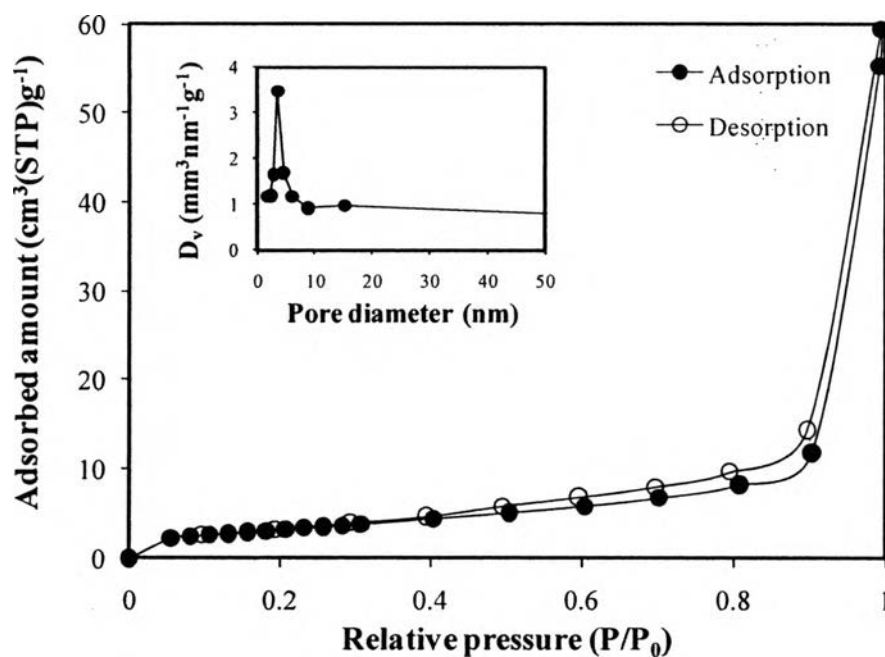
(c)

(d)

Figure 4.2 (Continued) N$_2$ adsorption-desorption isotherms and pore size distributions (insets) of the synthesized (a) SrTiO$_3$, (b) SrTi$_{0.9}$Zr$_{0.1}$O$_3$, (c) SrZrO$_3$ photocatalyst calcined at 700°C for 4 h, and (d) the synthesized 1.0 wt.% Pt-loaded SrTi$_{0.9}$Zr$_{0.1}$O$_3$ photocatalyst calcined at 850°C for 4 h.

Table 4.2 Summary of N_2 adsorption-desorption results of the synthesized mesoporous-assembled $SrTi_xZr_{1-x}O_3$ photocatalysts

Photocatalyst	Calcination temperature (°C)	Calcination time (h)	BET surface area(m^2g^{-1})	Mean mesopore diameter (nm)	Total pore volume (cm^3g^{-1})
SrTiO₃	600	4	16.0	8.8	0.044
	650		13.0	8.8	0.043
	700		9.9	3.6	0.043
	750		8.0	3.6	0.048
	800		7.0	3.6	0.053
SrTi₀.₉₅Zr₀.₀₅O₃	700	4	12.2	15.4	0.050
SrTi₀.₉Zr₀.₁O₃			22.2	15.6	0.105
SrTi₀.₈₅Zr₀.₁₅O₃			8.9	15.4	0.052
SrTi₀.₈Zr₀.₂O₃			10.6	15.7	0.051
SrTi₀.₇Zr₀.₃O₃			8.0	8.7	0.028
SrTi₀.₅Zr₀.₅O₃			4.1	4.6	0.012
SrZrO₃			3.0	_(a)	_(a)
SrTi₀.₉Zr₀.₁O₃	600	4	17.4	8.7	0.074
	650		17.7	8.8	0.074
	700		22.2	15.6	0.105
	750		13.0	15.6	0.072
	800		11.2	3.6	0.075
	700	2	20.9	15.5	0.092
		3	18.6	15.6	0.086
		4	22.2	15.6	0.105
		5	15.6	15.5	0.075
		6	23.5	15.6	0.102
		8	20.4	15.9	0.101

[a] N_2 adsorption-desorption isotherms correspond to an IUPAC type III-like pattern.

Table 4.3 Summary of N_2 adsorption-desorption results of the synthesized Pt-loaded mesoporous-assembled $SrTi_{0.9}Zr_{0.1}O_3$ photocatalysts with various Pt loading contents calcined at different calcination temperatures for 4 h

Photocatalyst	Pt loading content (wt.%)	Calcination temperature (°C)	BET surface area (m^2g^{-1})	Mean mesopore diameter (nm)	Total pore volume (cm^3g^{-1})
$SrTi_{0.9}Zr_{0.1}O_3$	0.0	700	22.2	15.6	0.105
	0.5	700	18.2	15.9	0.079
		750	11.3	15.8	0.066
		800	12.8	3.6	0.080
	0.7	700	14.7	15.7	0.062
		750	15.4	15.7	0.075
		800	13.8	3.6	0.080
	1.0	700	16.1	15.7	0.073
		750	18.5	15.9	0.095
		800	14.2	3.6	0.082
		850	12.0	3.6	0.086
		900	7.9	3.6	0.050
	1.2	750	18.8	2.3	0.091
		800	13.8	3.6	0.084
	1.5	750	17.1	3.6	0.087
		800	13.7	3.6	0.078

4.1.3 XRD Results

The X-ray analysis was used to identify the crystalline phases and purity of the synthesized photocatalysts. The XRD patterns of the synthesized mesoporous-assembled $SrTi_xZr_{1-x}O_3$ photocatalysts calcined at 700°C are shown in Figure 4.3. The dominant peaks at 2θ of about 32.4, 39.9, 46.4, 57.8, 67.8, and 77.2°, which represent the indices of (110), (111), (200), (211), (220), and (310) planes, respectively, could be indexed to the $SrTiO_3$ with a cubic perovskite structure (JCPDS card no. 35-0734) (Smith, 1960). The diffraction peaks of the $SrTiO_3$, as the most clearly seen for the (110) plane, gradually shifted to a lower angle with increasing Zr content, which could confirm the existence of zirconium in the form of solid solution in the synthesized $SrTi_xZr_{1-x}O_3$ photocatalysts. The synthesized $SrZrO_3$ photocatalyst could be identified as an orthorhombic structure from the appearance of the dominant peaks at 2θ of about 30.2, 30.9, 44.2, 50.4, and 55.0°, which represent the indices of (200), (121), (202), (301), and (321) planes, respectively (JCPDS card no. 44-0161) (Smith, 1960). The diffraction peak at 25.2°, which represents the index of $SrCO_3$ (111) plane, showed the presence of $SrCO_3$ impurity, which unavoidably coexisted in the resulting photocatalysts during the synthesis and calcination processes. It can be seen that a higher amount of $SrCO_3$ impurity was observed with increasing Zr content, indicating that the carbon atoms in the Zr precursor (ZRB) was difficult to remove from the gel network and tended to form the $SrCO_3$ compound. As seen in Figure 4.4, an increase in the calcination temperature caused an increase in both the purity and crystallinity of the synthesized $SrTiO_3$ and $SrTi_{0.9}Zr_{0.1}O_3$ photocatalysts (Puangpetch et al., 2008). However, from Figure 4.5, when the Pt co-catalyst with various loadings was deposited on the mesoporous-assembled $SrTi_{0.9}Zr_{0.1}O_3$ photocatalyst, the presence of the Pt phase was not clearly observed by the XRD analysis, which is probably due to its low contents with a high dispersion degree throughout the mesoporous-assembled network (Puangpetch et al., 2009). It can also be found that the $SrCO_3$ impurity tended to more coexist in the synthesized Pt-loaded $SrTi_{0.9}Zr_{0.1}O_3$ photocatalysts calcined at temperatures lower than 800°C.

The crystallite sizes of all the synthesized photocatalysts were estimated from the line broadening of the correlative X-ray diffraction peak of each crystalline phase by using the Sherrer equation (Cullity, 1978) (Eq. 4.1):

$$L = \frac{k\lambda}{\beta \cos(\theta)} \tag{4.1}$$

where L is the crystallite size, k is the Sherrer constant usually taken as 0.89, λ is the wavelength of the X-ray radiation (0.15418 nm for Cu Kα), β is the full width at half maximum (FWHM) of the diffraction peak measured at 2θ, and θ is the diffraction angle. The results summarized in Table 4.4 reveal that the crystallite sizes of the synthesized $SrTi_xZr_{1-x}O_3$ photocatalysts significantly decreased from 26 to 6 nm with increasing Zr content. In addition, it was observed that the crystallite sizes of the synthesized $SrTiO_3$ and $SrTi_{0.9}Zr_{0.1}O_3$ photocatalysts slightly increased with increasing calcination temperature, whereas a significant change of the crystallite sizes with increasing calcination time was not observed. From Table 4.5, the XRD results point out that the addition of Pt in the investigated range only slightly affected the crystallite size of the synthesized $SrTi_{0.9}Zr_{0.1}O_3$ photocatalyst.
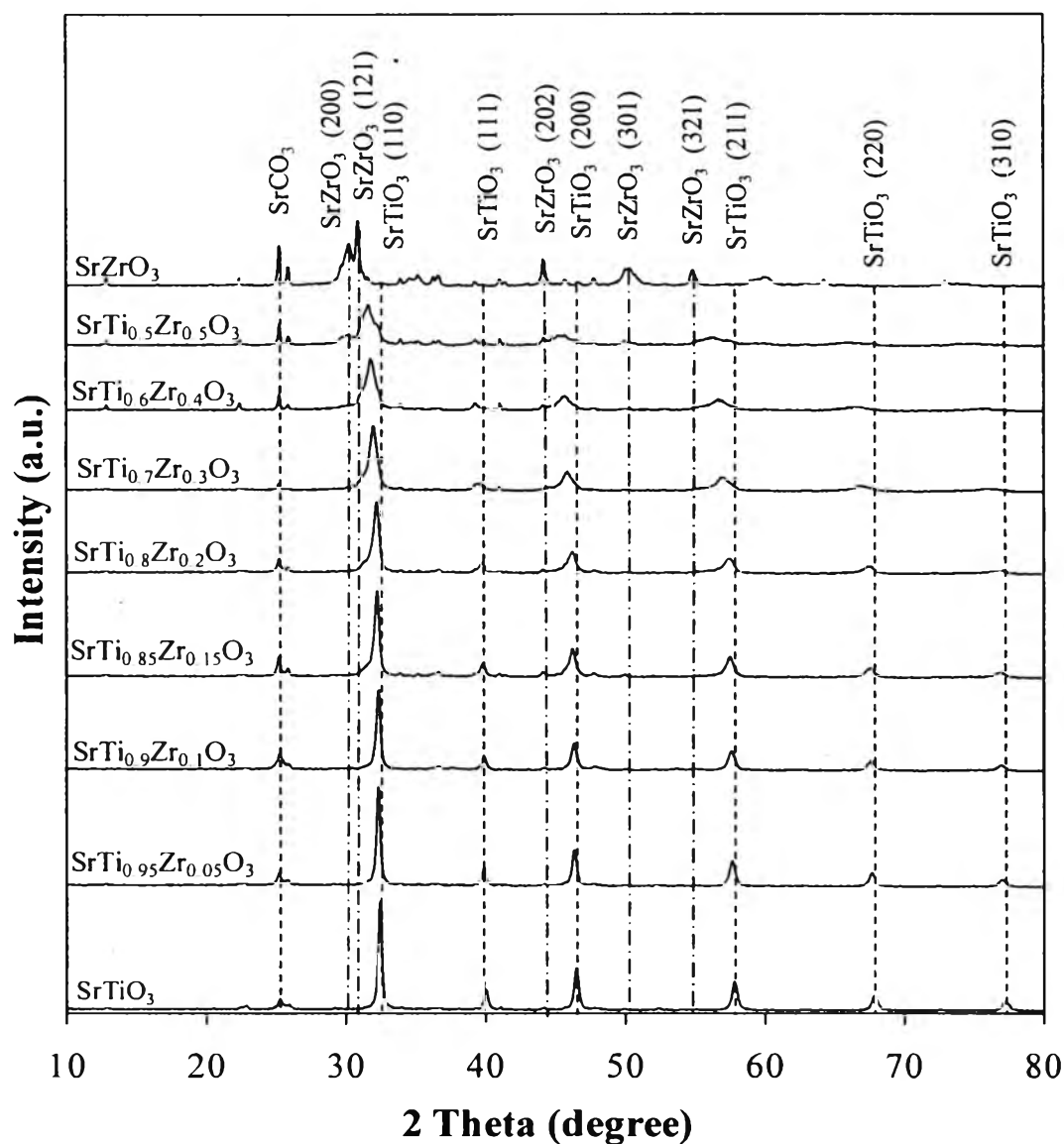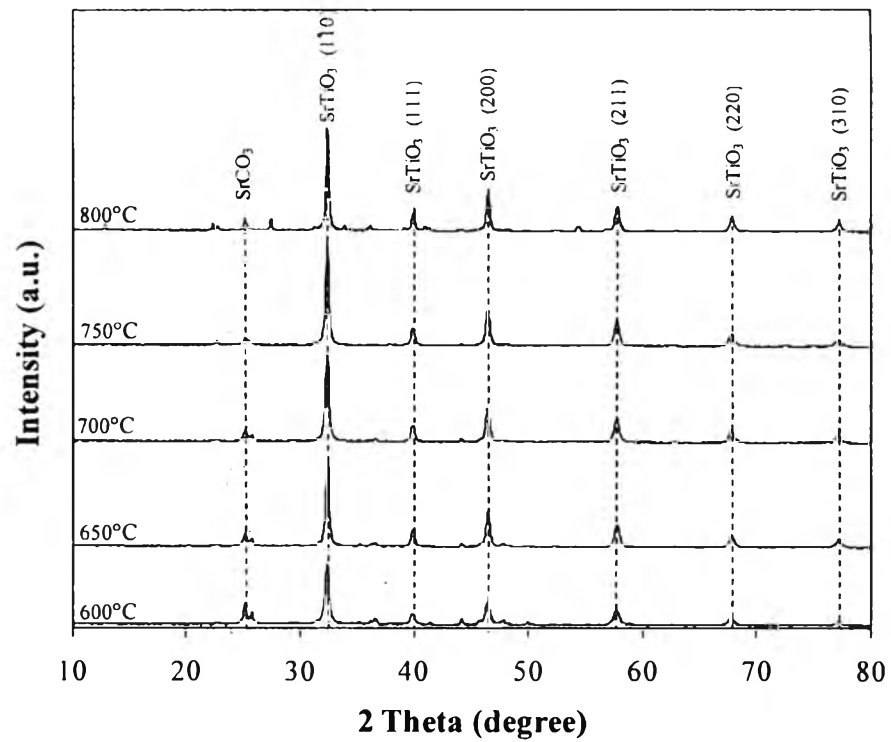
Figure 4.3 XRD patterns of the synthesized mesoporous-assembled $SrTi_xZr_{1-x}O_3$ photocatalysts calcined at 700°C for 4 h.
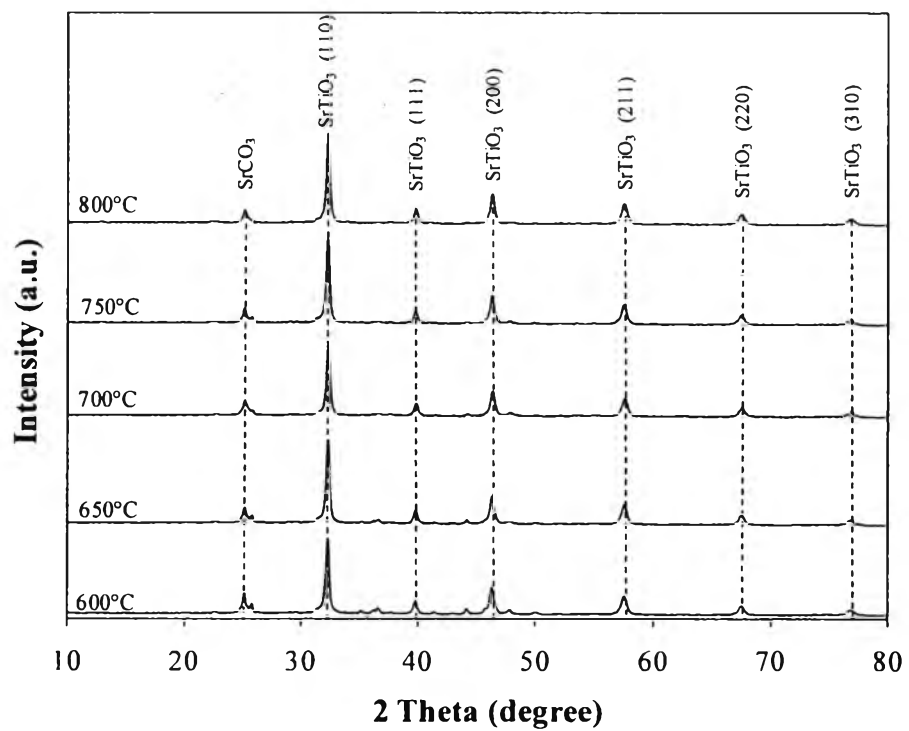
(a)

(b)

Figure 4.4 XRD patterns of the synthesized mesoporous-assembled (a) SrTiO₃ and (b) SrTi₀.₉Zr₀.₁O₃ photocatalysts calcined at various temperatures for 4 h.
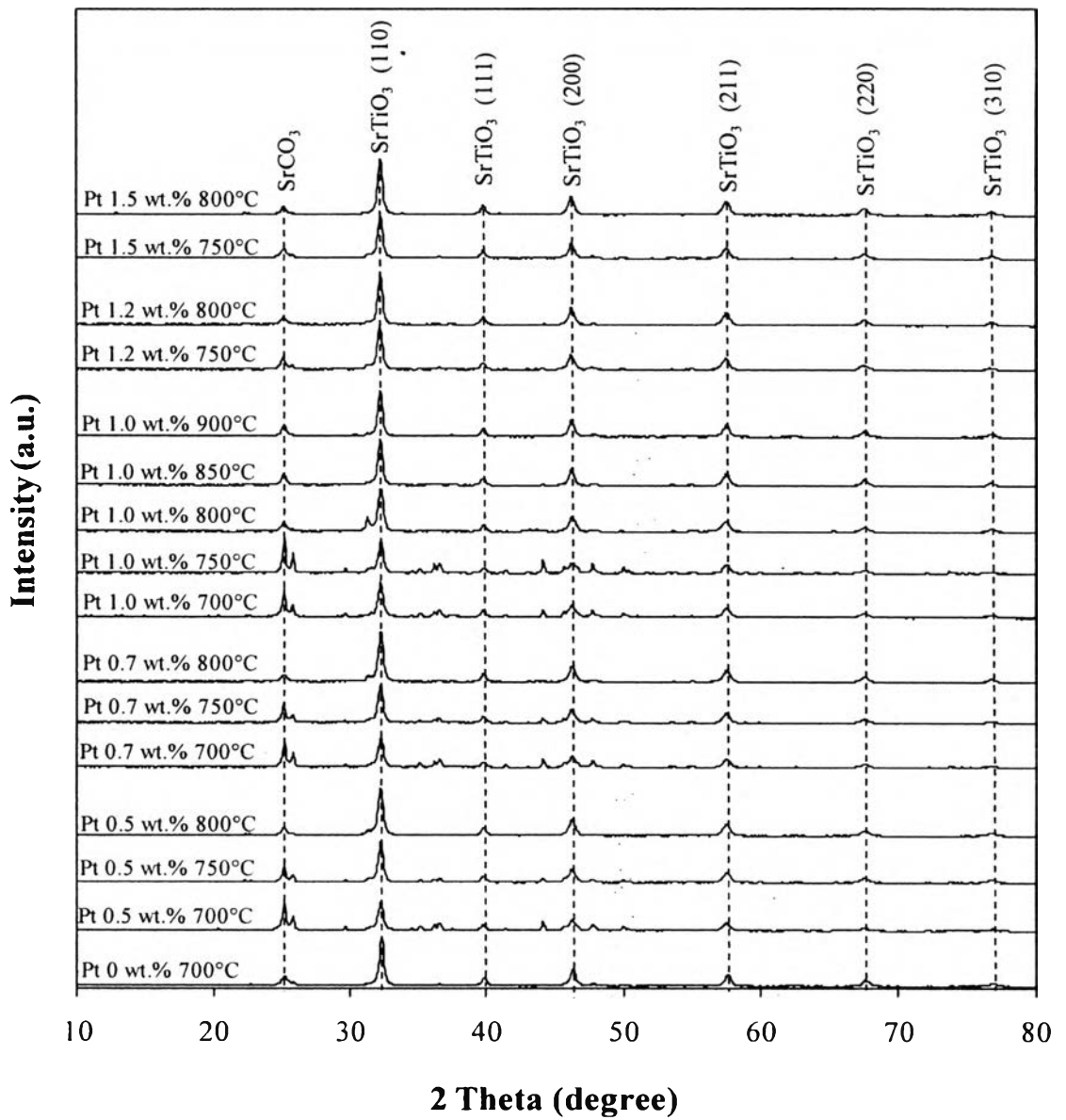
Figure 4.5 XRD patterns of the synthesized Pt-loaded mesoporous-assembled $SrTi_{0.9}Zr_{0.1}O_3$ photocatalysts with various Pt loadings calcined at various temperatures for 4 h.

Table 4.4 Summary of XRD analysis of the synthesized mesoporous-assembled $SrTi_xZr_{1-x}O_3$ photocatalysts calcined at various conditions

Photocatalyst	Calcination temperature (°C)	Calcination time (h)	Phase from XRD pattern	Crystallite size (nm)
SrTiO$_3$	600			20.5
	650			23.4
	700	4	Cubic	26.4
	750			27.7
	800			31.5
SrTi$_{0.95}$Zr$_{0.05}$O$_3$				24.8
SrTi$_{0.9}$Zr$_{0.1}$O$_3$				22.4
SrTi$_{0.85}$Zr$_{0.15}$O$_3$			Cubic	19.9
SrTi$_{0.8}$Zr$_{0.2}$O$_3$				14.9
SrTi$_{0.7}$Zr$_{0.3}$O$_3$	700	4		12.6
SrTi$_{0.6}$Zr$_{0.4}$O$_3$				9.2
SrTi$_{0.5}$Zr$_{0.5}$O$_3$			Cubic + Orthorhombic	6.4
SrZrO$_3$			Orthorhombic	5.6
	600			20.5
	650			21.5
	700	4		22.4
	750			23.4
	800			24.4
SrTi$_{0.9}$Zr$_{0.1}$O$_3$		2	Cubic	22.1
		3		22.4
	700	4		22.4
		5		20.5
		6		20.0
		8		21.5

Table 4.5 Summary of XRD analysis of the synthesized Pt-loaded mesoporous-assembled $SrTi_{0.9}Zr_{0.1}O_3$ photocatalysts with various Pt loadings calcined at various temperatures

| Photocatalyst	Pt loading content (wt.%)	Calcination temperature (°C)	Calcination time (h)	Phase from XRD pattern	Crystallite size (nm)
$SrTi_{0.9}Zr_{0.1}O_3$	0.0	700	4	Cubic	22.4
	0.5	700			18.6
		750			20.5
		800			20.5
	0.7	700			17.6
		750			18.8
		800			19.7
	1.0	700			18.6
		750			19.5
		800			18.2
		850			19.7
		900			20.5
	1.2	750			19.0
		800			20.0
	1.5	750			20.0
		800			20.5

4.1.4 UV-Visible Spectroscopy Results

UV-visible spectroscopy was used to examine the light absorption ability of all synthesized photocatalysts. The UV-visible spectra of the synthesized mesoporous-assembled $SrTi_xZr_{1-x}O_3$ calcined at 700°C, $SrTiO_3$ calcined at 600-800°C, $SrTi_{0.9}Zr_{0.1}O_3$ calcined at 600-800°C, and Pt-loaded $SrTi_{0.9}Zr_{0.1}O_3$ calcined at 800°C are shown in Figure 4.6. The results of absorption onset wavelength and corresponding band gap energy of all photocatalysts without and with Pt loading are summarized in Tables 4.6 and 4.7, respectively. It was observed that the absorption band of the synthesized $SrTi_xZr_{1-x}O_3$ photocatalysts was mainly in the UV light range of 200-400 nm, and the absorption onset wavelength shifted to shorter value with increasing Zr content and located between the absorption onset wavelengths of the $SrTiO_3$ and $SrZrO_3$ photocatalysts. The band gap energy (E_g, eV) of the mesoporous-assembled $SrTi_xZr_{1-x}O_3$ photocatalysts was in the range of 3.12-3.35 eV, which were obtained from extrapolating the onset of the rising part to x-axis (λ_g, nm) of the plots, as shown by dotted lines in Figure 4.6(a), and calculated by Eq. (4.2).

$$E_g = \frac{1240}{\lambda_g} \tag{4.2}$$

where λ_g is the wavelength (nm) of the exciting light. It can be seen that the band gap energies of the synthesized $SrTi_{0.9}Zr_{0.1}O_3$ and $SrTiO_3$ photocatalysts calcined in the temperature range of 600-800°C slightly decreased with increasing calcination temperature, whereas the calcination time did not affect the band gap energy of the $SrTi_{0.9}Zr_{0.1}O_3$ photocatalysts. For the Pt-loaded $SrTi_{0.9}Zr_{0.1}O_3$ photocatalysts, the Pt loading slightly increased the absorption onset wavelength of the $SrTi_{0.9}Zr_{0.1}O_3$ photocatalyst, leading to a gradual decrease in the band gap energy from 3.18 to 3.10 eV. These may be possibly because the presence of Pt on the $SrTi_{0.9}Zr_{0.1}O_3$ photocatalyst surface results in the formation of a Schottky barrier at Pt-$SrTi_{0.9}Zr_{0.1}O_3$ interface, which reduces the energy position of the $SrTi_{0.9}Zr_{0.1}O_3$ conduction band to its minimum potential level, leading to an observed decrease in the band gap energy of the synthesized $SrTi_{0.9}Zr_{0.1}O_3$ photocatalyst (Puangpetch *et al.*, 2009).

(a)
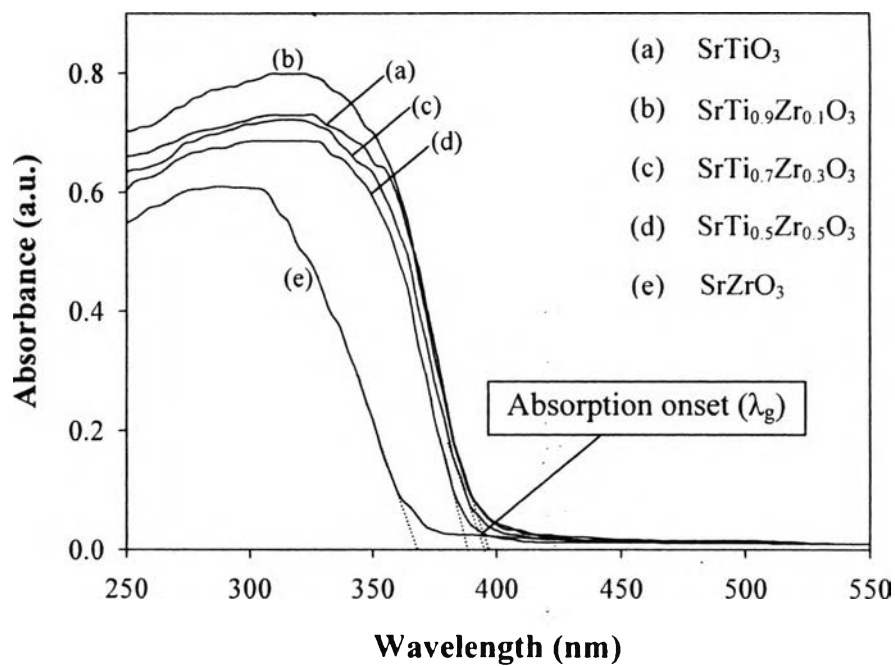
(b)

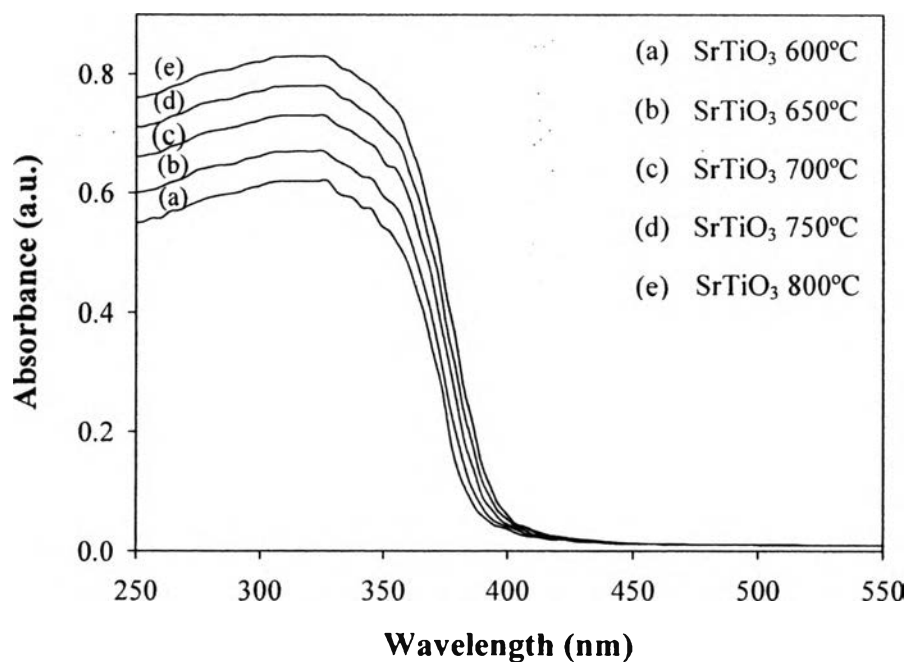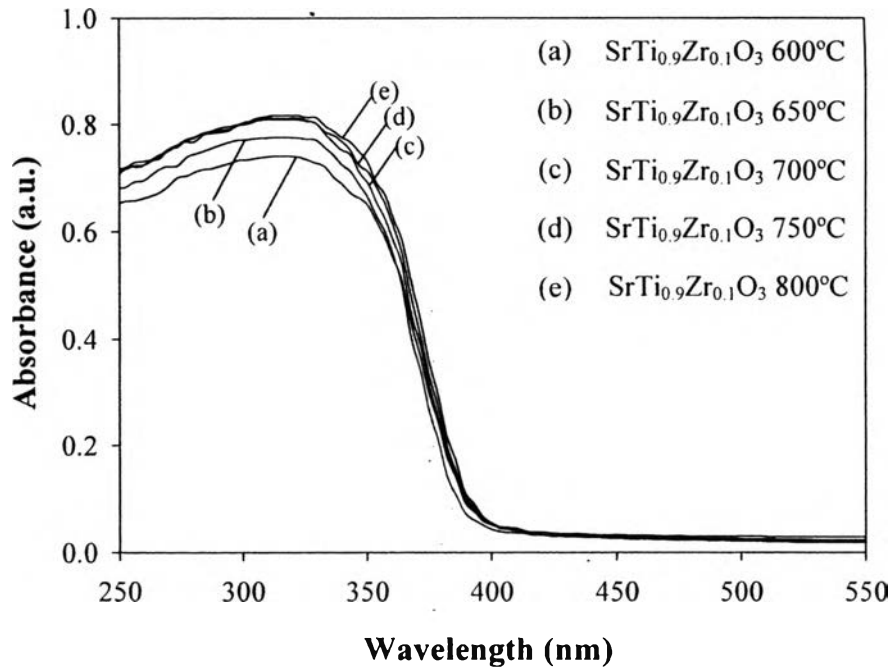**Figure 4.6** UV-visible spectra of the mesoporous-assembled photocatalysts: (a) SrTi$_x$Zr$_{1-x}$O$_3$ calcined at 700°C, (b) SrTiO$_3$ calcined at 600-800°C, (c) SrTi$_{0.9}$Zr$_{0.1}$O$_3$ calcined at 600-800°C, and (d) Pt-loaded mesoporous-assembled SrTi$_{0.9}$Zr$_{0.1}$O$_3$ calcined at 800°C.
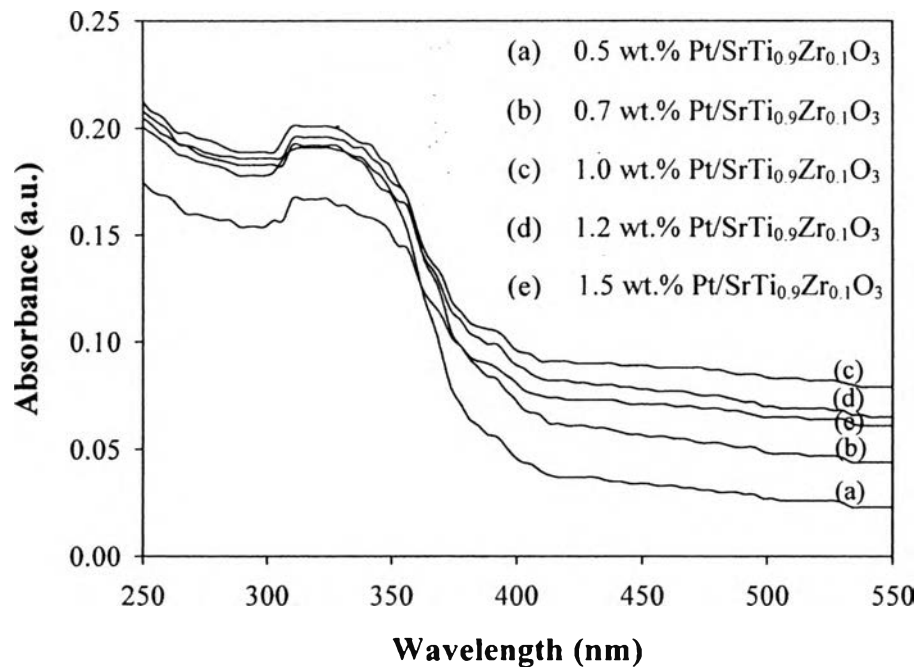
(c)

(d)

Figure 4.6 (Continued) UV-visible spectra of the mesoporous-assembled photocatalysts: (a) $SrTi_xZr_{1-x}O_3$ calcined at 700°C, (b) $SrTiO_3$ calcined at 600-800°C, (c) $SrTi_{0.9}Zr_{0.1}O_3$ calcined at 600-800°C, and (d) Pt-loaded mesoporous-assembled $SrTi_{0.9}Zr_{0.1}O_3$ calcined at 800°C.

Table 4.6 Summary of onset absorption wavelength and band gap energy obtained from UV-visible spectra of the synthesized mesoporous-assembled $SrTi_xZr_{1-x}O_3$ photocatalysts calcined at various conditions

| Photocatalyst	Calcination temperature (°C)	Calcination time (h)	Absorption wavelength, λ_g (nm)	Band gap energy (eV)
$SrTiO_3$	600		384	3.23
	650		386	3.21
	700	4	391	3.17
	750		396	3.13
	800		403	3.08
$SrTi_{0.95}Zr_{0.05}O_3$			391	3.17
$SrTi_{0.9}Zr_{0.1}O_3$			390	3.18
$SrTi_{0.85}Zr_{0.15}O_3$			389	3.19
$SrTi_{0.8}Zr_{0.2}O_3$	700	4	389	3.19
$SrTi_{0.7}Zr_{0.3}O_3$			388	3.20
$SrTi_{0.6}Zr_{0.4}O_3$			386	3.21
$SrTi_{0.5}Zr_{0.5}O_3$			384	3.23
$SrZrO_3$			368	3.37
$SrTi_{0.9}Zr_{0.1}O_3$	600		387	3.20
	650		389	3.19
	700	4	390	3.18
	750		394	3.15
	800		396	3.13
	700	2	390	3.18
		3		
		4		
		5		
		6		
		8		

Table 4.7 Summary of absorption onset wavelength and band gap energy obtained from UV-visible spectra of .the synthesized Pt-loaded mesoporous-assembled $SrTi_{0.9}Zr_{0.1}O_3$ photocatalysts with various Pt loadings calcined at various temperatures

Photocatalyst	Pt loading (wt.%)	Calcination temperature (°C)	Calcination time (h)	Absorption onset wavelength, λ_g (nm)	Band gap energy (eV)
$SrTi_{0.9}Zr_{0.1}O_3$		700	4	390	3.18
	0.5	700		390	3.18
		750		392	3.16
		800		393	3.16
	0.7	700		392	3.16
		750		393	3.16
		800		394	3.15
	1.0	700		392	3.16
		750		393	3.16
		800		395	3.14
		850		398	3.12
		900		401	3.09
	1.2	750		395	3.14
		800		398	3.12
	1.5	750		399	3.11
		800		400	3.10

4.1.5 SEM-EDX Results

The SEM images of the synthesized $SrTi_{0.9}Zr_{0.1}O_3$ and 1.0 wt.% Pt-loaded $SrTi_{0.9}Zr_{0.1}O_3$ photocatalysts are shown in Figures 4.7(a) and 4.8(a), respectively. The SEM images show that the quite uniform-size particles were observed in the form of aggregated clusters consisting of many nanoparticles. This nanoparticle aggregation can be possibly the cause of the mesoporous-assembled structure formation in the synthesized photocatalysts. The elemental distribution of the samples was investigated by the EDX mappings, as also shown in Figures 4.7(b) and 4.8(b). The white dots in each elemental mapping image show the existence and the distribution of all the investigated components (Sr, Ti, Zr, O, and Pt) in the photocatalyst samples. It can be clearly seen that all elements of the $SrTi_{0.9}Zr_{0.1}O_3$ and Pt-loaded $SrTi_{0.9}Zr_{0.1}O_3$ were well dispersed. The results imply that the photocatalyst preparation by the single-step sol-gel method provided a high distribution of the cocatalyst throughout the support (Sreethawong et al., 2005). A quantity of each element in the synthesized photocatalysts was also obtained by an analysis of the EDX elemental mapping, as summarized in Table 4.8. The results show that the number of mole of all components based on 1 mol of Sr in the photocatalyst molecular structure was nearly the same as that in its theoretical chemical formula. For the loaded Pt cocatalyst, the actual weight percentage of Pt loading in the 1.0 wt.% (nominal) Pt-loaded $SrTi_{0.9}Zr_{0.1}O_3$ was founded to be approximately 1.35.
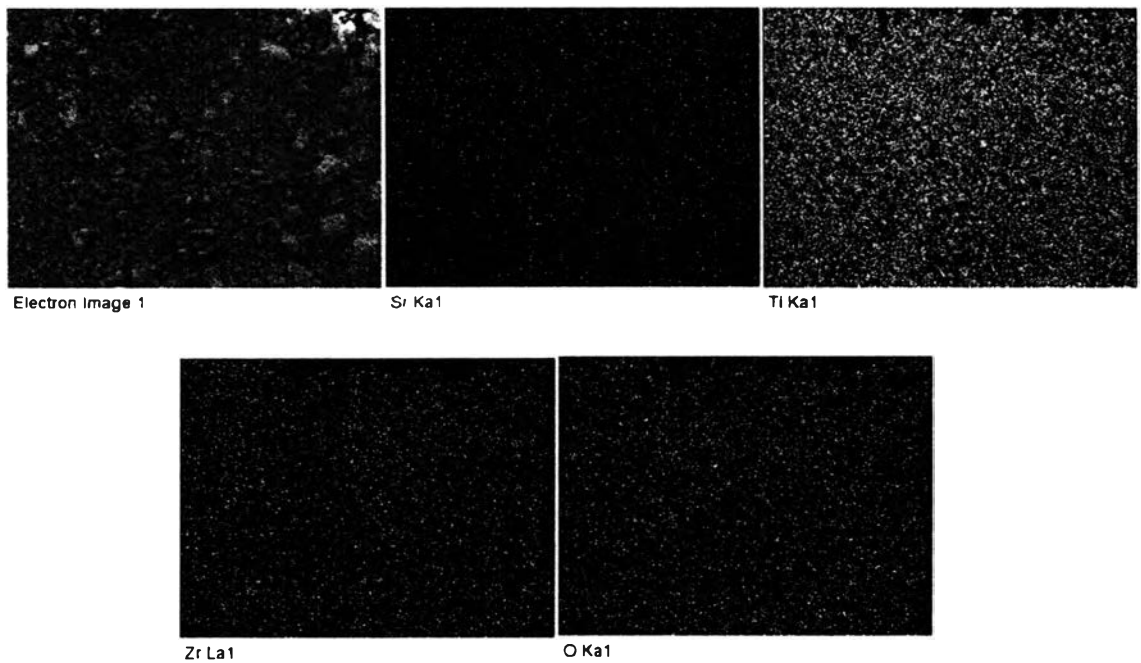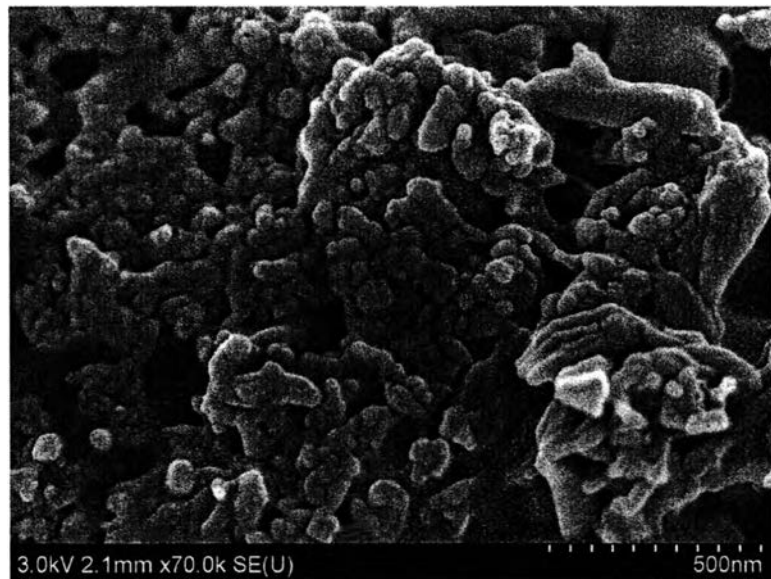
(a)
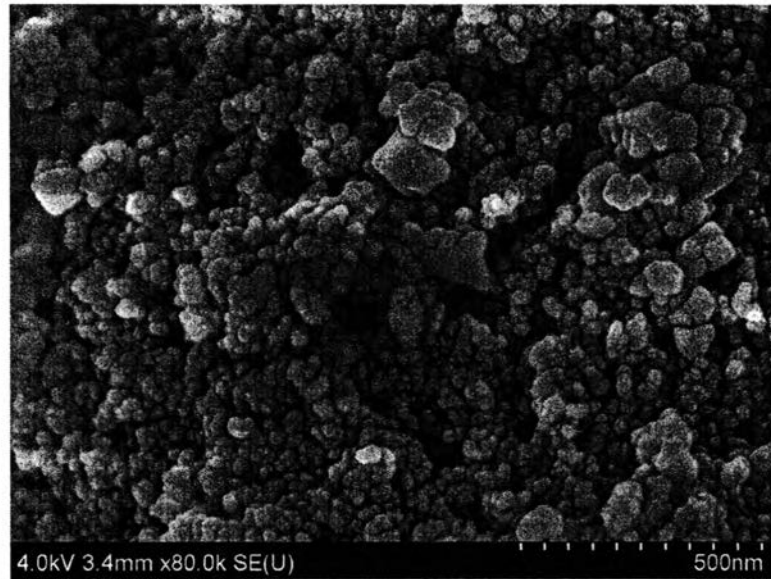
(b)

Figure 4.7 SEM image (a) and EDX area mappings (b) of the synthesized mesoporous-assembled $SrTi_{0.9}Zr_{0.1}O_3$ photocatalyst calcined at 700°C for 4 h.

(a)

3.0kV 2.1mm x70.0k SE(U)   500nm

(b)

Electron Image 1   Sr Ka1   Ti Ka1

Zr La1   O Ka1   Pt La1

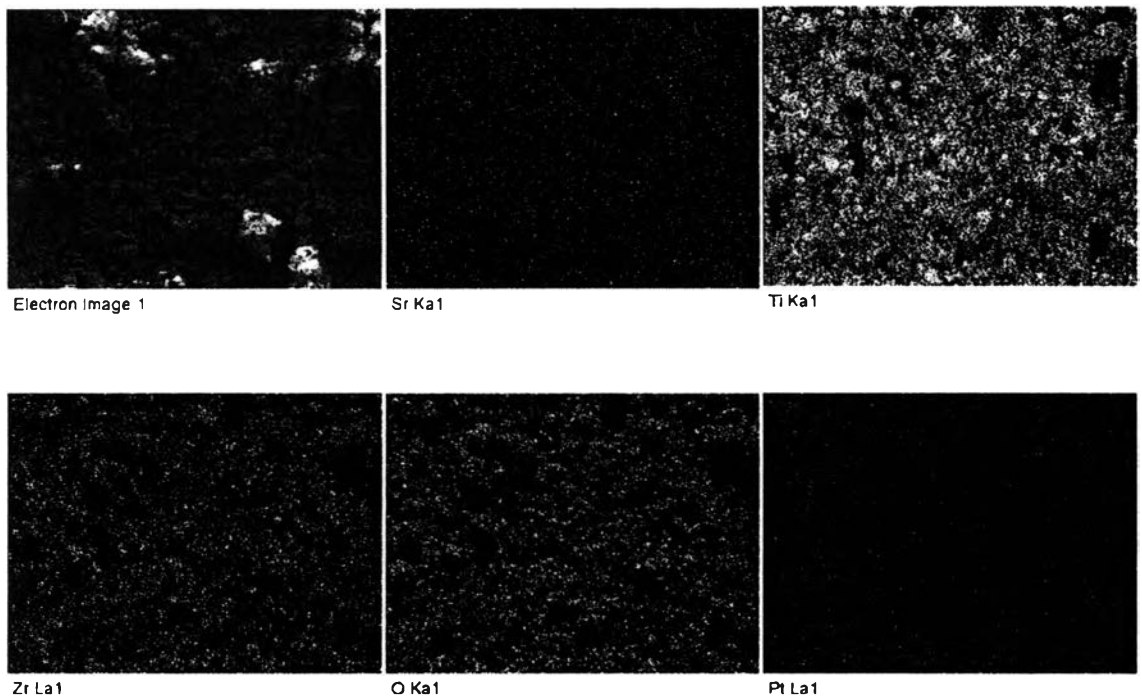**Figure 4.8** SEM image (a) and EDX area mappings (b) of the synthesized 1.0 wt.% Pt-loaded mesoporous-assembled $SrTi_{0.9}Zr_{0.1}O_3$ photocatalyst calcined at 800°C for 4 h.

Table 4.8 EDX elemental mapping of the mesoporous-assembled $SrTi_{0.9}Zr_{0.1}O_3$ photocatalyst calcined at 700°C and 1.0 wt.% Pt-loaded mesoporous-assembled $SrTi_{0.9}Zr_{0.1}O_3$ photocatalyst calcined at 800°C

Photocatalyst	Element	Weight percentage (%)	Molar percentage (%)	Number of mole[a]
$SrTi_{0.9}Zr_{0.1}O_3$	Sr	42.89	17.26	1.00
	Ti	19.52	14.38	0.83
	Zr	5.53	2.14	0.12
	O	30.06	66.23	3.84
1.0 wt.% Pt-loaded $SrTi_{0.9}Zr_{0.1}O_3$	Pt	1.35	0.24	0.01
	Sr	40.85	16.04	1.00
	Ti	20.86	15.00	0.93
	Zr	6.05	2.28	0.14
	O	30.89	66.44	4.14

[a] Based on 1 mol of Sr in the photocatalyst molecular structure

4.1.6 TEM-EDX Results

The morphologies and particle sizes of the synthesized photocatalysts, i.e. the $SrTiO_3$ calcined at 700°C, the $SrZrO_3$ calcined at 700°C, and the $SrTi_{0.9}Zr_{0.1}O_3$ calcined at 650-750°C, were investigated by the TEM analysis, as illustrated in Figure 4.9. The morphologies of the $SrTiO_3$ and $SrTi_{0.9}Zr_{0.1}O_3$ photocatalysts are the cubic shape, whereas that of the $SrZrO_3$ is the layer-like shape. The average particle sizes of the $SrTiO_3$ and $SrTi_{0.9}Zr_{0.1}O_3$ photocatalysts are in the range of 20-35 and 20-30 nm, respectively. However, the average particle size of the $SrZrO_3$ photocatalyst cannot be exactly given, due to its layered structure, and only its thickness range of 5-10 nm should be reported. These results showed that the particle sizes of the crystalline photocatalysts are similar to the crystallite sizes calculated from the XRD patterns by the Scherrer equation, indicating a single crystalline characteristic. Besides, the TEM and EDX mapping analyses of the synthesized 1.0 wt.% Pt-loaded mesoporous-assembled $SrTi_{0.9}Zr_{0.1}O_3$ photocatalyst calcined at 800°C was also performed. As shown in Figure 4.10, the existence of the Pt nanoparticles on the $SrTi_{0.9}Zr_{0.1}O_3$ photocatalyst was clearly observed, as confirmed by the EDX result. The average particle size of the Pt nanoparticles is approximately 15-20 nm.
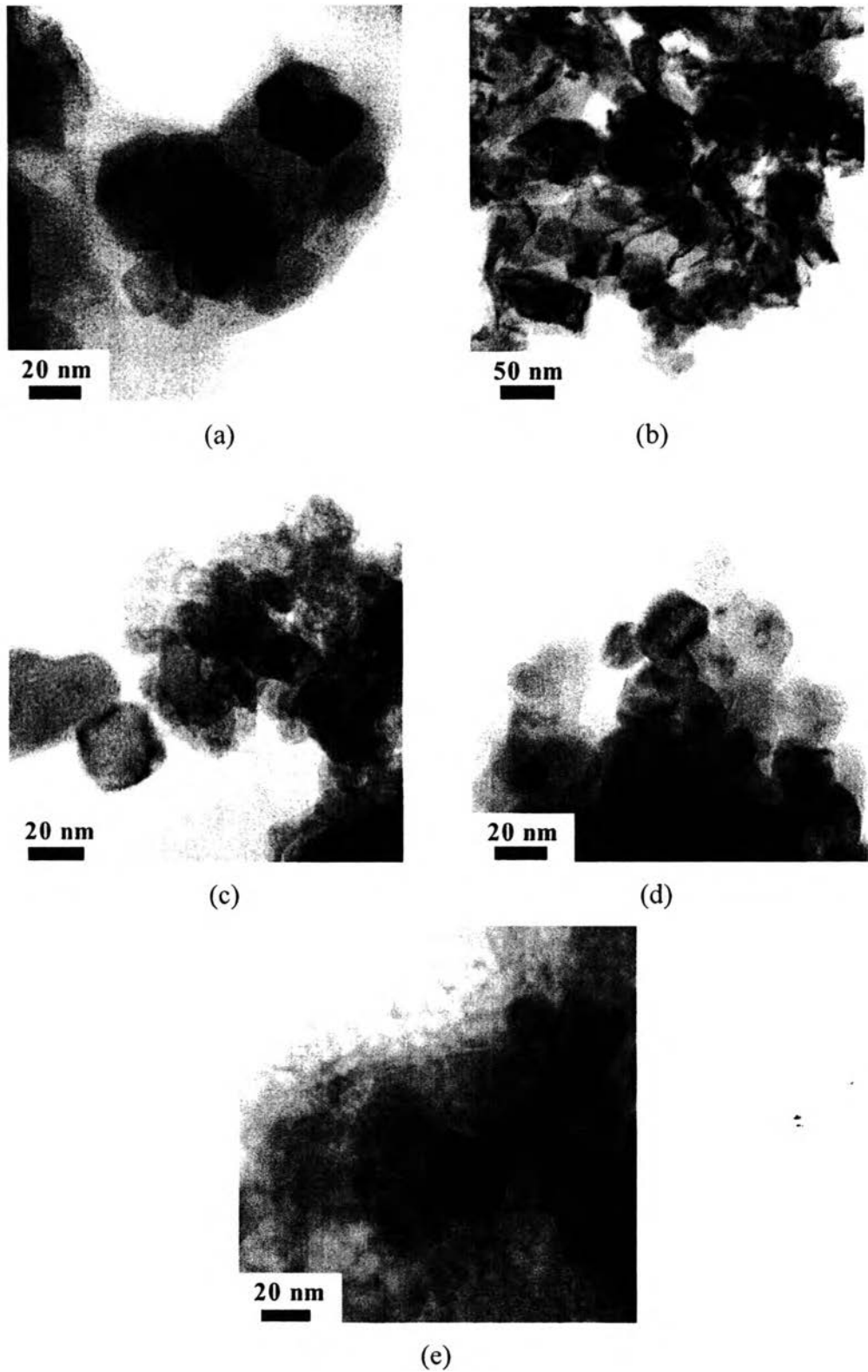
Figure 4.9 TEM images of the synthesized (a) $SrTiO_3$ calcined at 700°C, (b) $SrZrO_3$ calcined at 700°C, and (c,d,e) $SrTi_{0.9}Zr_{0.1}O_3$ photocatalysts calcined at 650, 700, 750°C, respectively.

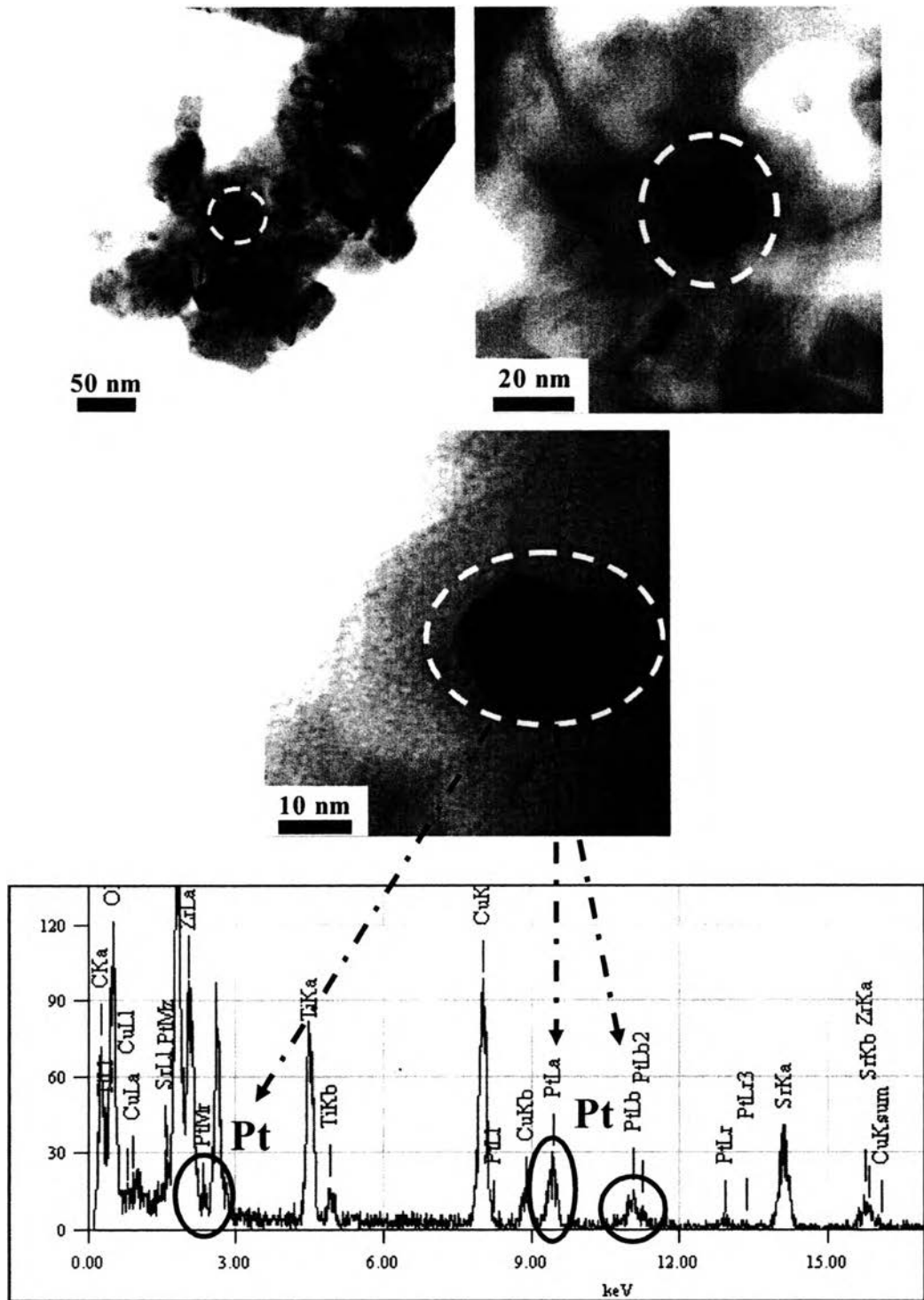**Figure 4.10** TEM images and EDX elemental point mapping of the 1.0 wt.% Pt-loaded mesoporous-assembled $SrTi_{0.9}Zr_{0.1}O_3$ photocatalyst calcined at 800°C.

4.1.7 TPR Results

The TPR analysis was carried out to study the reducibility of the loaded Pt species, as well as the interaction between support and loaded Pt. The TPR profiles of the $SrTi_{0.9}Zr_{0.1}O_3$ support without and with different Pt loadings and calcined at different temperatures, i.e. $SrTi_{0.9}Zr_{0.1}O_3$ calcined at 700°C, 0.7 wt.% Pt-loaded $SrTi_{0.9}Zr_{0.1}O_3$ calcined at 700°C, and 1.0 wt.% Pt-loaded $SrTi_{0.9}Zr_{0.1}O_3$ calcined between 750 and 900°C, are illustrated in Figure 4.11. It was clearly seen that the $SrTi_{0.9}Zr_{0.1}O_3$ support showed no reduction peak at temperatures lower than 350°C (the peaks at high temperatures can be assigned to the support reduction), whereas the Pt-loaded $SrTi_{0.9}Zr_{0.1}O_3$ exhibited a main reduction peak between 200 and 300°C. The reduction peak of the 0.7 wt.% Pt-loaded $SrTi_{0.9}Zr_{0.1}O_3$ calcined at 700°C was observed at about 235°C, which can be assigned to the reduction of Pt^{2+} to Pt^0, as also observed by Gonzalez *et al.* (2010) for the reduction of Pt in Pt/CeO_2 catalyst. Regardless of the Pt loading content in the calcination rage of 700-800°C, the position of the reduction peak gradually shifted to a higher temperature. It can also be observed that the reduction peak became broader with less intensity for the sample prepared at a higher temperature, even though a higher optimum Pt content was used (1.0 wt.%) at 750 and 800°C as compared to a lower optimum Pt content of 0.7 wt.% used for the sample prepared at a lower temperature of 700°C. The results imply the significant effect of calcination temperature on the phase of deposited Pt nanoparticles. It can be reasonably believed that at the calcination temperature of 800°C, only a very small portion of the loaded Pt was in the non-metallic form (Pt^{2+}), whereas a large portion was in the metallic form (Pt^0). With increasing calcination temperature from 700 to 750 and 800°C, the metallic portion gradually increased due to the smallr reduction peak of the Pt-loaded sample calcined at a higher temperature. As it was proposed that with using a sol-gel method, the loaded metal oxides can be reduced by some thermally decomposed species generated during the calcination of organic precursors (Aristizabal *et al.*, 2004), this corresponds well with the observed results in this work (where the examples of thermally decomposed species were CO and NH_3) that the calcination at a higher temperature of 800°C yielded a higher portion of metallic Pt, which in turn, results in a higher interaction with the support. However, when the calcination temperature further increased from 800 to 850°C, a

small portion of Pt nanoparticles may be re-oxidized to be the non-metallic form, resulting in an observed higher intensity of the reduction peak at about 235°C. The result suggests that the organic precursors used for the investigated sol-gel method released the thermally decomposed species when increasing calcination temperature up to only 800°C, and there were no such species released at a higher temperature due to their complete decomposition at 800°C. This resulted in a higher possibility of some surface Pt fractions to be re-oxidized. Interestingly, when further increasing calcination temperature to 900°C, the reduction peak again became broader with less intensity, observed at a temperature a little bit lower than 235°C. A possible reason is that at this too high calcination temperature, the significant agglomeration of Pt nanoparticles occurred, also with less interaction of the agglomerated Pt with the support. This can be clearly confirmed by the Pt dispersion result as shown in the next section.
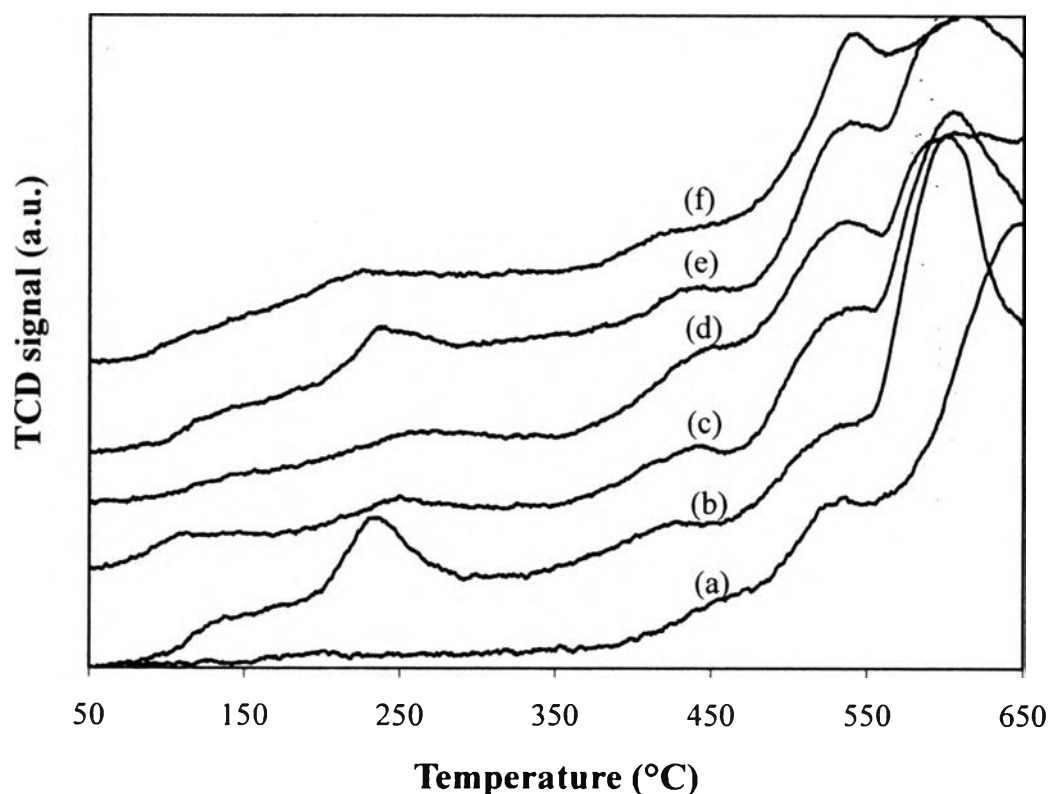

Figure 4.11 TPR profiles of (a) the synthesized $SrTi_{0.9}Zr_{0.1}O_3$ calcined at 700°C, (b) 0.7 wt.% Pt-loaded $SrTi_{0.9}Zr_{0.1}O_3$ calcined at 700°C, (c,d,e,f) 1.0 wt.% Pt-loaded $SrTi_{0.9}Zr_{0.1}O_3$ calcined at 750°C, 800°C, 850°C, and 900°C.

4.1.8 H₂ Chemisorption Results

The H_2 chemisorption analysis was used to determine the Pt dispersion, as well as the agglomeration of the Pt nanoparticles. The results of Pt dispersion of all Pt-loaded photocatalysts are summarized in Table 4.9. It can be seen that the Pt dispersion at all Pt loadings in the range of 0.5-1.0 wt.% tended to increase with increasing calcination temperature from 700 to 800°C. However, the substantial decrease in the Pt dispersion of the 1.0 wt.% Pt-loaded $SrTi_{0.9}Zr_{0.1}O_3$ photocatalyst calcined at temperatures higher than 800°C (i.e. 850 and 900°C) was observed, possibly because of the Pt nanoparticle agglomeration at too high calcination temperatures, as above mentioned.

Table 4.9 Summary of Pt dispersion results of the synthesized Pt-loaded mesoporous-assembled $SrTi_{0.9}Zr_{0.1}O_3$ photocatalysts with various Pt loadings calcined at various temperatures

Photocatalyst	Pt loading content (wt.%)	Calcination temperature (°C)	Dispersion (%)
$SrTi_{0.9}Zr_{0.1}O_3$	0.5	700	13.86
		750	23.62
		800	24.85
	0.7	700	17.06
		750	26.57
		800	35.14
	1.0	700	20.85
		750	31.39
		800	41.25
		850	28.88
		900	16.63
	1.2	750	16.58
		800	21.89
	1.5	750	16.68
		800	21.48

4.2 Photocatalytic AB Degradation Results

UV-visible spectroscopy was used to investigate the AB dye degradation performance of the synthesized mesoporous-assembled $SrTi_xZr_{1-x}O_3$ photocatalysts. The UV-visible spectrum of AB solution revealed the maximum absorbance wavelength (λ_{max}) value at 619 nm, as shown in Figure 4.12. This absorbance can be attributed to the $\pi \rightarrow \pi^*$ transition related to the azo group (–N=N–), which represents the color of the AB dye (Sun *et al.*, 2007). Therefore, the decrease in this λ_{max} value was used to evaluate the AB dye degradation performance in terms of decolorization.
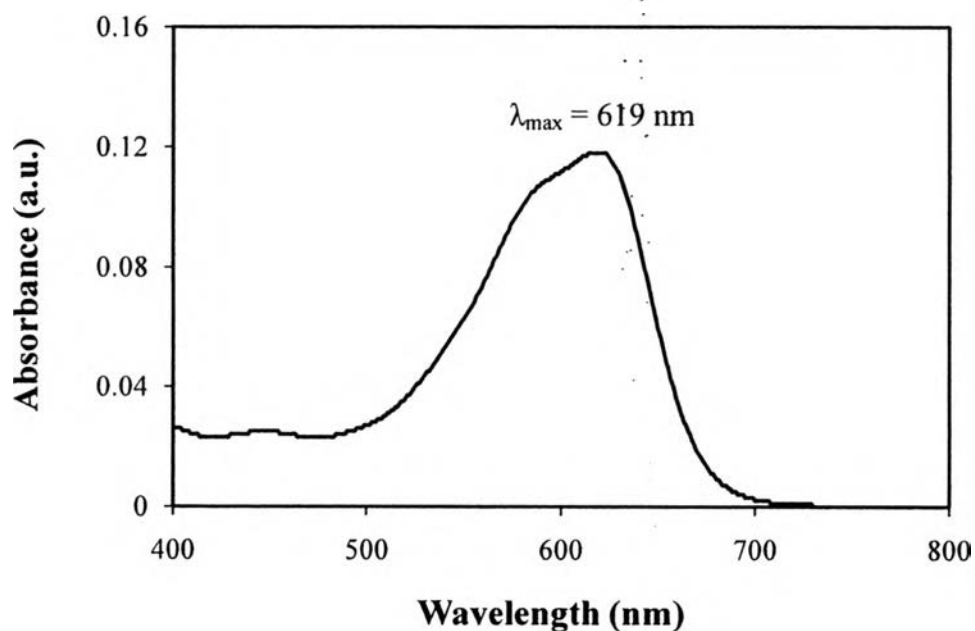

Figure 4.12 UV-visible spectrum of AB dye solution.

4.2.1 Effect of Ti-to-Zr Molar Ratio

In this study, the mesoporous-assembled $SrTi_xZr_{1-x}O_3$ photocatalysts synthesized at various Ti-to-Zr molar ratios (as expressed by x in the $SrTi_xZr_{1-x}O_3$ where x = 0-1) and calcined at 700°C were used to investigate the photocatalytic AB degradation performance in order to find the suitable Ti-to-Zr molar ratio. It must be first noted that experiments performed without either any photocatalyst or light irradiation showed no change in the AB dye absorbance, indicating that the AB degradation did not occur. The results of photocatalytic AB degradation at various Ti-to-Zr molar ratios the terms of reaction rate constant (k) are shown in Figure 4.13. It can be clearly seen that the synthesized $SrTi_{0.9}Zr_{0.1}O_3$ (with 90 mol% Ti and 10 mol% Zr) photocatalyst provided the higher reaction rate constant than the other synthesized $SrTi_xZr_{1-x}O_3$ photocatalysts. The observed photocatalytic activity results can be possibly explained by the BET surface area results (Table 4.2), showing the highest value for the $SrTi_{0.9}Zr_{0.1}O_3$ photocatalyst. This indicated that this photocatalyst possessed higher surface active reaction sites and lower probability of matual e^-/h^+ recombination than the others, leading to its higher photocatalytic activity. However, it was clearly observed that the reaction rate constant significantly decreased with further increasing Zr content (decreasing x in the $SrTi_xZr_{1-x}O_3$) to become closed to $SrZrO_3$. These results may be possibly because the Zr-rich $SrTi_xZr_{1-x}O_3$ photocatalysts had a too wide band gap energy (Table 4.6), leading to a more difficult electron excitation to the conduction band and accordingly causing a decreased photocatalytic activity. From the XRD results (Table 4.4), it can be also noticed that more Zr addition over 10 mol% (x < 0.9) led to smaller crystallite sizes of the photocatalysts, resulting in higher probability of matual e^-/h^+ recombination at both surface and bulk traps (Sreethawong *ea al.*, 2005). In addition, the lack of mesoporous structure in the synthesized $SrZrO_3$ is believed to provide less reactant accessibility to its surface for the photocatalytic reaction. In contrast, the synthesized $SrTi_{0.9}Zr_{0.1}O_3$ with a uniform pore size and a high crystallinity could decrease the number of lattice defects and then facilitate the electron and hole transport for reacting with water and/or oxygen molecules adsorbed on its surface along the mesoporous structure to create many active species, such as $OH^•$ and $O_2^{•-}$ (Jantawasu *et al.*, 2009). Therefore, the synthesized $SrTi_{0.9}Zr_{0.1}O_3$ photocatalyst was selected for

further experiments to investigate the effects of calcination temperature and calcination time.

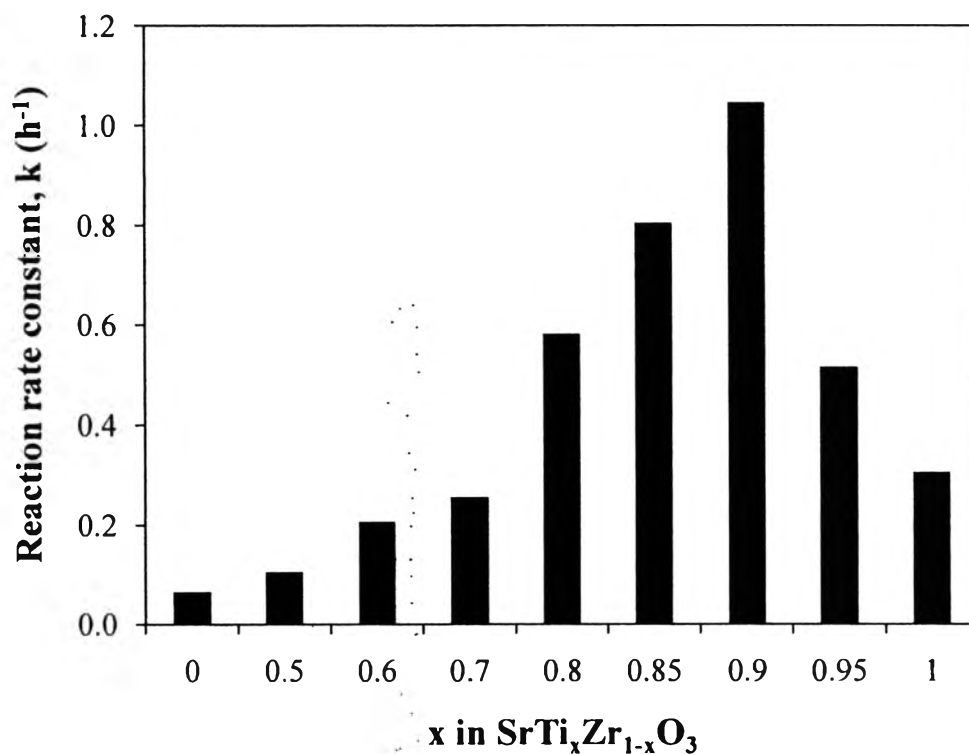**Figure 4.13** Effect of Ti-to-Zr molar ratio of the synthesized mesoporous-assembled $SrTi_xZr_{1-x}O_3$ photocatalyst calcined at 700°C on the AB degradation performance in terms of reaction rate constant (Photocatalyst, 0.5 g; total volume, 100 ml; initial AB concentration 15 mg/l; irradiation time, 4 h).

4.2.2 Effect of Calcination Temperature

The effect of calcination temperature of the synthesized mesoporous-assembled $SrTi_{0.9}Zr_{0.1}O_3$ photocatalyst on the photocatalytic AB degradation was next investigated. The photocatalytic activity results of the $SrTi_{0.9}Zr_{0.1}O_3$ photocatalyst as compared to the $SrTiO_3$ photocatalyst calcined at various temperatures between 600 and 800°C are shown in Figure 4.14(a). It was found that the reaction rate constant of the AB dye over the $SrTi_{0.9}Zr_{0.1}O_3$ photocatalyst increased substantially and reached a maximum value at 700°C; however, when the calcination temperature exceeded 700°C, the reaction rate constant decreased. The similar trend was also observed for the $SrTiO_3$ photocatalyst. These results indicated

that the calcination temperature strongly affected the photocatalytic activity of AB degradation. These can be explained by using both the BET surface area and the crystallinity, which were directly governed by the calcination temperature, as clearly seen in Table 4.2 and Figure 4.4, respectively, where the explanation for this observation can be divided into two regions of the calcination temperature. Firstly, for the calcination temperature in the range of 600 to 700°C, the increase in the temperature led to increases in both the crystallinity and specific surface area, which resulted in increasing the photocatalytic activity of both the photocatalysts, where the increase in the photocatalytic activity resulted from the positive effect of the increased crystallinity (less number of lattice defects) might exceed the negative effect of the decreased specific surface area. Secondly, for the calcination temperature in the range of 700 to 800°C, the increase in the temperature led to a slight increase in the crystallinity but to a significant decrease in the specific surface area. Therefore, the decrease in the photocatalytic activity of both the photocatalysts in this temperature range possibly resulted from the drastic reduction of the specific surface area (Puangpetch et al., 2008). From the comparative photocatalytic activity tests, the synthesized $SrTi_{0.9}Zr_{0.1}O_3$ photocatalyst provided much significantly higher AB degradation performance than the synthesized $SrTiO_3$ photocatalyst over the entire range of investigated calcination temperature. When considering the reaction rate constant enhancement (Figure 4.14(b)), which was calculated from the Eq. (4.3):

$$\text{Reaction rate constant enhancement (\%)} = \frac{k_{SrTi_{0.9}Zr_{0.1}O_3} - k_{SrTiO_3}}{k_{SrTiO_3}} \times 100 \qquad (4.3)$$

The results showed that the reaction rate constant enhancement of the $SrTi_{0.9}Zr_{0.1}O_3$ as compared to the $SrTiO_3$ increased with increasing calcination temperature and reached the maximum value around 252% at the calcination temperature of 750°C. Although the reaction rate constant enhancement showed the maximum value at 750°C (but only slightly higher than at 700°C), the photocatalytic activity at this temperature (750°C) was moderately lower than that at 700°C. Therefore, the calcination temperature of 700°C was considered as the optimum value to be used in further experiments.
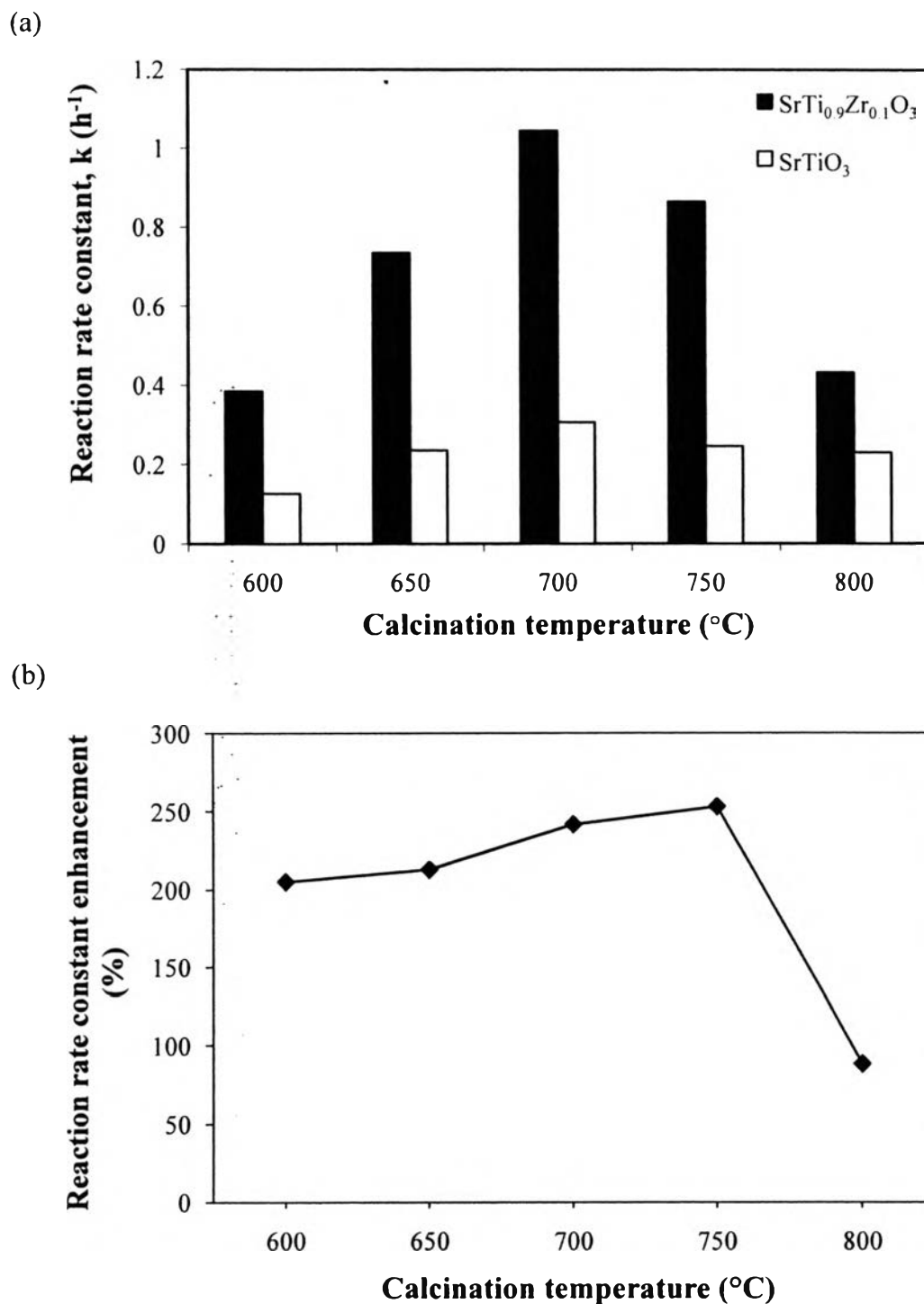
(a)

(b)

Figure 4.14 Effect of calcination temperature of the synthesized mesoporous-assembled $SrTi_{0.9}Zr_{0.1}O_3$ and $SrTiO_3$ photocatalysts calcined for 4 h on (a) the AB degradation performance in terms of reaction rate constant and (b) reaction rate constant enhancement (Photocatalyst, 0.5 g; total volume, 100 ml; initial AB concentration 15 mg/l; irradiation time, 4 h).

4.2.3 Effect of Calcination Time

From literature review, it was found that the photocatalytic activity of a photocatalyst also depends on the calcination time. Thus, in this work, various calcination times ranging from 2 to 8 h were used for the photocatalytic investigation in order to obtain the optimum value for calcining the synthesized mesoporous-assembled $SrTi_{0.9}Zr_{0.1}O_3$ photocatalyst. The photocatalytic AB degradation results of the $SrTi_{0.9}Zr_{0.1}O_3$ photocatalyst calcined at 700°C for different calcination times are shown in Figure 4.15. It was clearly observed that the $SrTi_{0.9}Zr_{0.1}O_3$ photocatalyst calcined for 4 h provided a much higher AB degradation than that calcined for other times. This can be explained in that, in case of the calcination times shorter than 4 h (i.e. 2 and 3 h), an increase in the calcination time led to a smaller specific surface area of the photocatalyst, whereas a higher crystallinity was conversely observed. The increment of photocatalytic activity in this range of calcination time may be resulted from the superior effect of an increased crystallinity in facilitating the induced charge transfer. However, in case of increasing calcination time over 4 h, the photocatalytic activity abruptly decreased. This may be attributed to the dominant negative effect of the decrease in surface area, which accordingly resulted in the less number of active surface reaction sites and subsequently less reactant accessibility for the photocatalytic reaction (Sreethawong et al., 2005). Therefore, the calcination time of 4 h was selected for further use in the photocatalytic activity improvement.
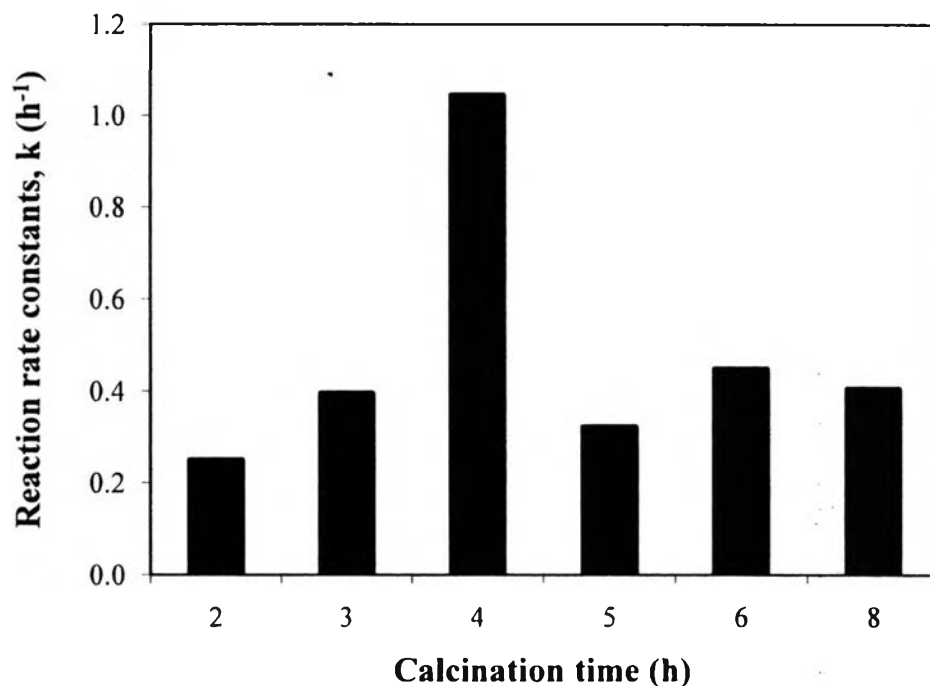
Figure 4.15 Effect of calcination time of the synthesized mesoporous-assembled $SrTi_{0.9}Zr_{0.1}O_3$ photocatalyst calcined at 700°C on the AB degradation performance in terms of reaction rate constant (Photocatalyst, 0.5 g; total volume, 100 ml; initial AB concentration 15 mg/l; irradiation time, 4 h).

4.2.4 Effect of Pt Loading

The synthesized mesoporous-assembled $SrTi_{0.9}Zr_{0.1}O_3$ photocatalyst was used for further investigation on the effect of Pt co-catalyst loading in the range of 0.5-1.5 wt.% prepared by the single-step sol-gel (SSSG) method on the photocatalytic AB degradation, while the Pt-loaded $SrTi_{0.9}Zr_{0.1}O_3$ photocatalysts were calcined at various temperatures. The results of the photocatalytic AB degradation in terms of reaction rate constant of the Pt-loaded $SrTi_{0.9}Zr_{0.1}O_3$ photocatalysts calcined at different temperatures are shown in Figure 4.16. It was clearly found that the Pt loading on the $SrTi_{0.9}Zr_{0.1}O_3$ photocatalyst could enhance the photocatalytic activity. This may be because the Pt nanoparticles loaded on the $SrTi_{0.9}Zr_{0.1}O_3$ surface can both help accelerate the electron transfer and act as an electron sink after band gap excitation in order to prevent the recombination between the photogenerated electron–hole pairs. The electrons can accumulate on the Pt

nanoparticles and then quickly react with O_2 molecules dissolved in the reaction solution, while the holes can react effectively with H_2O molecules. These suggested that the redox reactions to generate several active species, e.g. $O_2^{\cdot-}$, $OH^{\cdot}$, and $OH_2^{\cdot}$, can occur more easily, resulting in an observed enhancement of the photocatalytic activity. In the case of various Pt loadings at the calcination temperature of 700°C, the reaction rate constant slightly increased with increasing Pt loading up to 0.7 wt.%, and then it adversely decreased with further increasing Pt loading, whereas at the calcination temperatures of 750 and 800°C, the reaction rate constant also showed the same trend as that at calcination temperature of 700°C, but the highest reaction rate constant was found at the Pt loading of 1.0 wt.%. Since the highest reaction rate constant of 2.38 h^{-1} was observed for the 1.0 wt% Pt-loaded $SrTi_{0.9}Zr_{0.1}O_3$ photocatalyst calcined at 800°C, the optimum Pt loading for the present investigated system was considered in overall to be 1.0 wt.%. For an excessive Pt loading (higher than 1.0 wt.%), the observed decrease in the photocatalytic activity can be explained in that too much Pt addition resulted in a higher probability of the Pt nanoparticles to undesirably behave as recombination centers, and this consequently led to a marked increase in the recombination frequency between the photogenerated electrons and holes because the average distance between trapping sites decreases by increasing the number of Pt nanoparticles confined within a photocatalyst particle (Sreethawong *et al.*, 2006). As clearly seen in Figure 4.16(a), when increasing calcination temperature from 700 to 750 and 800°C, the photocatalytic activity at each corresponding optimum Pt loading (0.7 wt.% for 700°C and 1.0 wt.% for 750 and 800°C) significantly increased probably because a larger content of metallic Pt (Pt^0) and a higher Pt dispersion were attained at a higher calcination temperature, as explained above in the TPR and H_2 chemisorption results. Therefore, the photocatalyst with an optimum Pt loading of 1.0 wt.% was selected to study the effect of calcination temperature, especially higher than 800°C. The photocatalyst activity results shown in Figure 4.16(b) indicated that the calcination temperature of 850°C provided the highest reaction rate constant at about 3 h^{-1}. Although the Pt dispersion of the 1.0 wt.% Pt-loaded sample calcined at 850°C was less than that at 800°C (Table 4.9), the observed higher photocatalytic activity at 850°C may be because of higher interaction between the loaded Pt and $SrTi_{0.9}Zr_{0.1}O_3$ support at this calcination

temperature, possibly resulted from the complete removal of the thermally decomposed species from the photocatalyst surface, as mentioned in the TPR results.

Conclusively, it has to be emphasized that under the optimum Pt loading of 1.0 wt.% at the suitable calcination temperature of 850°C, the photocatalytic degradation rate constant of the mesoporous-assembled $SrTi_{0.9}Zr_{0.1}O_3$ photocatalyst was significantly enhanced from 1.05 (without Pt loading) to 3.00 h^{-1}.
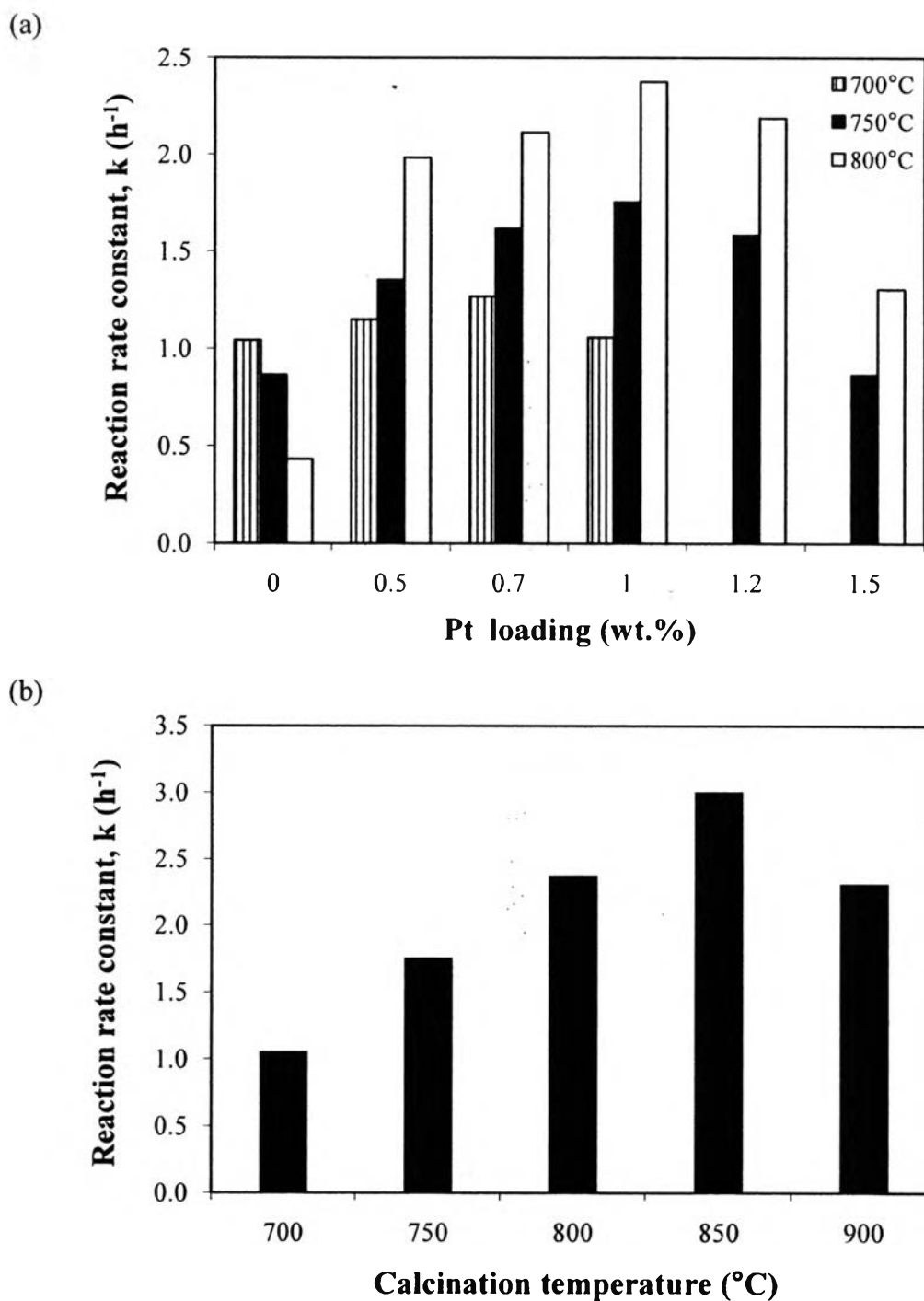
Figure 4.16 AB degradation performance in terms of reaction rate constant: (a) the effect of Pt loading for the synthesized Pt-loaded mesoporous-assembled $SrTi_{0.9}Zr_{0.1}O_3$ photocatalysts calcined at various temperatures and (b) the effect of calcination temperature for the 1.0 wt.% Pt-loaded $SrTi_{0.9}Zr_{0.1}O_3$ photocatalysts (Photocatalyst, 0.5 g; total volume, 100 ml; initial AB concentration 15 mg/l; irradiation time, 4 h).